



RESEARCH ARTICLE

10.1029/2022MS003473

Key Points:

- The stochastic unified convection scheme (UNICON) is extended to deep convection by parameterizing the impact of mesoscale organized flow
- The free parameters of stochastic UNICON are optimized using single-column model simulations over the ocean
- The biases presented in the simulations of original UNICON are reduced by stochastic UNICON for tropical deep convection

Supporting Information:

Supporting Information may be found in the online version of this article.

Correspondence to:

J.-J. Baik,
jjbaik@snu.ac.kr

Citation:

Shin, J., & Baik, J.-J. (2023). Optimization and evaluation of stochastic unified convection using single-column model simulations at multiple observation sites. *Journal of Advances in Modeling Earth Systems*, 15, e2022MS003473. <https://doi.org/10.1029/2022MS003473>

Received 18 OCT 2022
Accepted 28 APR 2023

Optimization and Evaluation of Stochastic Unified Convection Using Single-Column Model Simulations at Multiple Observation Sites

Jihoon Shin¹  and Jong-Jin Baik¹ 

¹School of Earth and Environmental Sciences, Seoul National University, Seoul, South Korea

Abstract We extend the previously developed stochastic unified convection scheme (UNICON) for shallow convection to deep convection by parameterizing the impact of mesoscale organized flow on updraft properties. The extended stochastic UNICON parameterizes thermodynamic properties of updrafts at the near-surface as a multivariate Gaussian distribution, where the variances of the distribution are the summation of variances from non-organized turbulence and mesoscale organized flow. The distribution of updraft radius is parameterized as a power-law distribution with a scale break which is parameterized as a linear function of the strength of mesoscale organized flow. The proposed parameterization is validated using a series of large-eddy simulations of deep convection. The free parameters introduced in the formulation of stochastic UNICON are optimized using 10 cases of single-column model simulations over the ocean. Stochastic UNICON with the optimized parameters significantly reduces the biases of thermodynamic profiles and surface precipitation rates simulated in the original UNICON for tropical convection cases. The simulation of the variation in anomalies of temperature and moisture associated with the Madden-Julian oscillation is also improved. The overall improvements in simulated thermodynamic profiles are found to be due to the increased heating and drying tendencies by convective processes in stochastic UNICON. An additional simulation of an idealized deep convection case shows that stochastic UNICON produces enhanced cloud variabilities with dependency on updraft radius, indicating its ability to represent the coexistence of shallow and deep convection.

Plain Language Summary The previously developed stochastic unified convection scheme (UNICON) is extended to deep convection in this study. Mesoscale organized flow driven by evaporation of convective precipitation promotes deep convection by increasing the variances of thermodynamic variables and horizontal sizes of convective updrafts at the near-surface. The extended stochastic UNICON simulates a spectrum of updrafts by launching updrafts from a joint probability density function (PDF), where the variances of the joint PDF are increased by mesoscale organized flow. The free parameters introduced in the formulation of stochastic UNICON are optimized using single-column model simulations over the ocean. Stochastic UNICON with the optimized parameters significantly reduces the errors in the simulations of original UNICON and also improves the simulation of the Madden-Julian oscillation.

1. Introduction

A main issue in convection parameterization is to represent the impact of ensembles of convective clouds within a model grid. A widely used simplification to this problem is the bulk plume approach which considers a single entraining plume. The bulk plume based mass flux schemes have been extensively used in operational atmospheric models due to their computational efficiency (Bechtold et al., 2008; Kain & Fritsch, 1990; Tiedtke, 1989). However, the bulk plume based mass flux schemes have a limitation on expressing different types of convective clouds since a single plume is used to represent the ensemble mean of multiple convective clouds. Another type of scheme, such as the Arakawa-Schubert scheme (Arakawa & Schubert, 1974), considers multiple convective updrafts with different cloud-top heights (Pan & Randall, 1998; G. Zhang & McFarlane, 1995). However, their quasi-equilibrium closures are known to be unsuitable for simulating shallow convection (Yano & Plant, 2020). For these reasons, many modelers use separate shallow and deep convection schemes to express the coexistence of shallow and deep convection.

Recently, there have been attempts to develop convection parameterizations that are capable of representing a spectrum of convective clouds without using separate schemes for different cloud types (Baba, 2019; Neggers, 2015; Suselj et al., 2019; Yang et al., 2021; Yoshimura et al., 2015). Global simulations with these schemes have shown

improvements in both the mean state and variability of the simulated global atmospheric circulation, particularly in the intensity and frequency of the simulated Madden-Julian oscillation (MJO). The spectral representation of convection has been found to contribute to reproducing the moisture supply from shallow convection to sustain organized convection (Baba, 2021; Baba & Giorgetta, 2020). This supports the importance of shallow convection in preconditioning the lower troposphere for developing the MJO, as investigated in many studies (Cai et al., 2013; Janiga & Zhang, 2016). Furthermore, Lawrence and Rasch (2005) showed that spectral representation of convection parameterization can enhance the efficiency of vertical transport of tropospheric tracers.

While several spectral convection parameterizations have been successfully implemented in general circulation models (GCMs), there is still a lack of understanding of how variability between convective clouds is formed. One of the most important factors generating the cloud variability is an entrainment rate, and many different parameterizations have been proposed (Dawe & Austin, 2013; Gregory, 2001; Kain & Fritsch, 1990; Lu et al., 2016; Neggers et al., 2002). However, an accurate entrainment formula that can be applied simultaneously to both shallow and deep convection is still an area of research (Baba, 2019). In addition, proper convective closure is required to simulate realistic transitions between different cloud types. Traditional convective closures based on a quasi-equilibrium assumption inevitably lose the memory of the cloud properties between the model time steps. This lack of memory seems to be one reason that conventional diagnostic convection schemes fail to simulate a realistic diurnal cycle of precipitation. This motivates the parameterization of mesoscale organized flow and its impact on convection. Mesoscale organized flow is also important in that it enhances the variabilities of convective clouds. A large-eddy simulation (LES) study of Kurowski et al. (2018) demonstrated that mesoscale organized flow greatly increases cloud variabilities by increasing the standard deviation of near-surface thermodynamic variables and reducing the entrainment rate of clouds. This implies that the enhanced cloud variabilities in the deep convection regime are generated by multiple physical processes and manifested as a joint distribution of multiple cloud properties.

A more general approach for representing multiple types of convection is based on constructing a joint probability density function (PDF) of convective clouds. Shin and Park (2020) developed a stochastic unified convection scheme (stochastic UNICON) for shallow convection with convective updraft plumes at the near-surface randomly sampled from the joint PDF for updraft thermodynamic scalars and updraft radius. The cloud variabilities above the near-surface are generated in a physical way with a sophisticated entrainment/detrainment rate parameterization. The study showed that this scheme produces a spectrum of convective updrafts that matches closely to the LES results in the case of shallow convection. They also proposed a method of emulating the stochastic fluctuation of convective tendencies in an equilibrium state from the joint PDF and a plume number distribution. The scheme is based on unified convection scheme (UNICON; Park (2014)), which simulates subgrid mesoscale organized flow and its impacts on subgrid convection in an explicit way.

The stochastic UNICON of Shin and Park (2020) does not simulate deep convection since it considers convective updrafts originating from non-organized turbulence. In this study, we extend stochastic UNICON to deep convection by parameterizing the increased variabilities of convective updraft properties by mesoscale organized flow. The multivariate distribution of thermodynamic variables and updraft radius at the near-surface is parameterized as a function of the strength of mesoscale organized flow. Four free parameters are introduced in the formulation of stochastic UNICON, and they are optimized using single-column model (SCM) simulations at multiple observation sites. It is best practice to optimize unknown model parameters using a number of global model simulations. However, the optimization problems regarding global simulations are complicated because a single evaluation of an objective function is expensive and it is usually hard to calculate the gradient of the objective function, so a number of evaluations are unavoidable (Neelin et al., 2010). Therefore, this study proposes an optimization method using SCM simulations, which are much cheaper to compute, of diverse cloud types, including stratus, stratocumulus, shallow convection, and deep convection. This procedure will provide provisional parameter values for global model simulations. Recently, an increasing number of studies have utilized a SCM to calibrate the parameters in their parameterizations (Couvreur et al., 2021; De La Chevrotiere et al., 2014; Hourdin et al., 2021; Langhans et al., 2019; Pathak et al., 2021). Hourdin et al. (2021) showed that the optimization of a 3D GCM can be accelerated by reducing parameter space with a SCM tuning procedure, and Pathak et al. (2021) demonstrated that the performance of a host GCM is considerably improved with the model parameters calibrated using a SCM. The performance of stochastic UNICON will be evaluated over the SCM cases, focusing on how the stochastic closure changes the characteristics of simulated convection. Particularly, MJO simulated in the Dynamics of the Madden-Julian Oscillation (DYNAMO) case is analyzed in detail. In addition,

the cloud variabilities simulated by stochastic UNICON in a near-equilibrium are evaluated with an idealized tropical convection case. Section 2 provides a formulation for stochastic UNICON extended to deep convection. Section 3 validates the proposed parameterization using LES simulations. Section 4 provides the settings of the SCM. Section 5 presents the strategy and results of optimization, and Section 6 provides the results from SCM simulations. Finally, a summary and conclusions are given in Section 7.

2. Stochastic Unified Convection Scheme for Deep Convection

2.1. Thermodynamic Variables

UNICON calculates thermodynamic properties of convective updrafts at the near-surface, assuming that they are perturbed from grid-mean values by non-organized turbulence and the mesoscale organized flow driven by cold pools. For non-organized turbulence, perturbations are determined by surface fluxes with assumed Gaussian distributions. UNICON parameterizes cold pools by solving prognostic equations for the net fractional area (a_{cp}) and the mean conservative scalars of cold pools (Equations 61–64 in Park (2014)). The prognostic treatment of cold pools generates convective memory between the model time steps. The cold pools in UNICON are defined as a portion in the planetary boundary layer (PBL) where buoyancy is less than a certain threshold. The inflows and outflows on cold pools are the source and sink of a_{cp} , and the fluxes at cold pool boundaries control the mean properties of cold pools. The main inflow to cold pools is convective downdrafts driven by the evaporation of precipitation (see Section 2d in Park (2014) for a detailed derivation of the prognostic equations). From the prognosed cold pool properties, perturbations of thermodynamic scalars of a convective updraft driven by the cold pools at the near-surface, $\Delta\phi_{\Omega}$, are calculated at each time step (see Appendix A). The strength of mesoscale organized flow is represented by the mesoscale organization parameter Ω , which is defined as

$$\Omega = \frac{a_{cp}}{1 - \hat{A}_{max}}, \quad 0 \leq \Omega \leq 1 \quad (1)$$

where \hat{A}_{max} is the maximum updraft fractional area and specified as 0.1. Ω plays a similar role to *org* parameter from Mapes and Neale (2011) in that it represents the strength of mesoscale organization with a prognosed variable. However, there is a difference in that UNICON also prognoses other thermodynamic properties of mesoscale organized flow and their impact on convective updrafts.

The thermodynamic properties of a bulk convective updraft at the near-surface in original UNICON are derived as

$$\hat{\phi} = \sigma_{\phi}\alpha_{\hat{\phi}} + \bar{\phi}_s + \Delta\phi_{\Omega}, \quad \phi = w, \theta_c, q_l, u, v, \xi \quad (2)$$

where σ_{ϕ} is the standard deviation, $\bar{\phi}_s$ is the grid-mean value at the near-surface, and $\alpha_{\hat{\phi}}$ is the normalized perturbation of ϕ . w is the vertical velocity; $\theta_c \equiv \theta - (L_v/c_p/\pi)q_l - (L_s/c_p/\pi)q_i$ is the condensate potential temperature, where θ is the potential temperature, L_v and L_s are the latent heats of vapourization and sublimation, respectively, c_p is the specific heat at constant pressure, and π is the Exner function; $q_t \equiv q_v + q_l + q_i$ is the total water specific humidity, where q_v , q_l , and q_i are the specific humidity of water vapor, liquid, and ice, respectively; u is the zonal wind speed; v is the meridional wind speed; ξ is the mass or number concentration of aerosols and chemical species.

Original UNICON uses a single bulk plume and utilizes a constant value for $\alpha_{\hat{\phi}}$ with the assumption that inter-variable correlations are 1. Then, $\hat{\phi}$ becomes a deterministic value depending on surface fluxes and the state of cold pools. Stochastic UNICON extends original UNICON by constructing a joint PDF of thermodynamic variables of convective updrafts at the near-surface and initiating multiple convective plumes with randomly sampled $\hat{\phi}$ from the joint PDF.

Shin and Park (2020) proposed a method of constructing a joint PDF of properties of updrafts by non-organized turbulence at the near-surface from the surface-layer similarity theory. The vertical velocity and thermodynamic scalars of convective updrafts at the near-surface are randomly sampled from the multivariate Gaussian distribution, where standard deviations and inter-variable correlations are derived from the surface-layer similarity theory. The standard deviations are obtained using the following similarity functions:

$$\sigma_w/u_* = \phi_{\sigma_w}\left(\frac{z}{L}\right) = 1.25\left(1.0 - 3\frac{z}{L}\right)^{1/3}, \quad (3)$$

$$\sigma_\theta/\theta^* = \phi_{\sigma_\theta}\left(\frac{z}{L}\right) = -2.0\left(1.0 - 8\frac{z}{L}\right)^{-1/3}, \quad (4)$$

$$\sigma_q/q^* = \phi_{\sigma_q}\left(\frac{z}{L}\right) = -2.4\left(1.0 - 8\frac{z}{L}\right)^{-1/3}, \quad (5)$$

where z is the geometric height, $u_* = \left[\left(\overline{w'u'}\right)_s^2 + \left(\overline{w'v'}\right)_s^2\right]^{1/4}$ is the frictional velocity, $\theta^* = -\left(\overline{w'\theta'}\right)_s/u_*$, and $q^* = -\left(\overline{w'q'}\right)_s/u_*$. $\left(\overline{w'\theta'}\right)_s$, $\left(\overline{w'q'}\right)_s$, $\left(\overline{w'u'}\right)_s$, and $\left(\overline{w'v'}\right)_s$ are the kinematic surface fluxes of sensible heat, water vapor, zonal momentum, and meridional momentum, respectively, by non-organized symmetric turbulent eddies, and L is the Monin-Obukhov length scale (Hereafter, q denotes the water vapor specific humidity, q_v). The correlations can then be calculated as

$$r_{w\theta} = \left(\overline{w'\theta'}\right)_s/(\sigma_w\sigma_\theta) = -1/(\phi_{\sigma_w}\phi_{\sigma_\theta}), \quad (6)$$

$$r_{wq} = \left(\overline{w'q'}\right)_s/(\sigma_w\sigma_q) = -1/(\phi_{\sigma_w}\phi_{\sigma_q}), \quad (7)$$

$$|r_{\theta q}| = |r_{wq}|/|r_{w\theta}| = |\phi_{\sigma_\theta}/\phi_{\sigma_q}| = 0.83. \quad (8)$$

The standard deviations and correlations for other variables are also defined in Shin and Park (2020) (σ_i and r_{ij} , respectively, where $i, j = w, \theta, q, u, v, \xi$).

As mentioned in the introduction, mesoscale organized flow increases the variances of near-surface thermodynamic variables and greatly enhances cloud variabilities. The increased variances of near-surface thermodynamic variables due to mesoscale organized flow are parameterized by exploiting the cold pool computation in UNICON. We set the final joint PDF as multivariate Gaussian where the variance of each thermodynamic variable is summation of variances from non-organized turbulence and mesoscale organized flow. It is based on the assumptions that non-organized turbulence and mesoscale organized flow are uncorrelated stochastic processes and that the two stochastic processes determine the joint PDF of thermodynamic variables. In addition, the variance from mesoscale organized flow is assumed to be proportional to $(\Delta\phi_\Omega)^2$. The total standard deviation of thermodynamic scalar of updrafts at the near-surface σ_ϕ^* is parameterized as

$$\sigma_\phi^* = \sqrt{c_1\sigma_\phi^2 + c_2(\Delta\phi_\Omega)^2}, \quad (9)$$

where c_1 and c_2 are tunable parameters. The LES experiment from Shin and Park (2020) demonstrated that convective updrafts are formed by the merging of near-surface air parcels. If the merging occurs in a totally random manner, updrafts statistics become identical to near-surface turbulence statistics, so $c_1 = 1$. However, it is more likely that the merging process is dependent on the thermodynamic properties of air parcels (e.g., buoyant air parcels are more likely to merge), so c_1 ($0 < c_1 \leq 1$) is introduced to describe the effect of reduced variance when the near-surface air parcels coalesce to form convective updrafts. c_2 controls how much the mean perturbation by mesoscale organized flow increases the variance of updrafts. Although c_1 and c_2 may be physically parameterized, they are set as free parameters as we need a better understanding of how the convective updraft and mesoscale organized flow statistics are formed. The final thermodynamic properties of convective updrafts at the near-surface are derived as

$$\hat{\phi} = \sigma_\phi^*\alpha_\phi + \bar{\phi}_s, \quad (10)$$

where α_ϕ is a random sample from a standard multivariate Gaussian with the correlation matrix of r_{ij} , assuming that the correlation matrix is the same as that derived from the similarity theory.

Currently, the PDFs of near-surface thermodynamic variables are assumed as symmetric Gaussian, but in reality, the PDFs are close to skewed Gaussian in the presence of cold pools (e.g., Figure S3 in Supporting Information S1). In addition, the correlation between non-organized turbulence and mesoscale organized flow

may need to be considered in Equation 9, as mesoscale organized flow modulates surface fluxes. We need an advanced model for simulating the statistics of mesoscale organized flow to avoid these assumptions.

2.2. Updraft Radius

Studies examining cloud size statistics for various cloud types have shown that the number density of cloud size follows a power-law distribution with a scale break (Heus & Seifert, 2013; Neggers et al., 2003; O'Brien et al., 2013; Wood & Field, 2011). Based on this, Shin and Park (2020) parameterizes the number density PDF of updraft radius R at the near-surface, P_n , as

$$P_n(\hat{x})/N = a_1 \hat{x}^{-2-\hat{x}^{1.7}}, \quad \int_0^\infty (P_n(\hat{x})/N) d\hat{x} = 1, \quad (11)$$

where $\hat{x} = R/R_b$ is the updraft plume radius normalized by the scale break radius R_b , N is the total updraft number density in unit of $[\# \text{ m}^{-2}]$, and a_1 is a normalization constant.

The scale break radius R_b sets an approximate upper limit for the possible plume size in a given environment. Although the factors controlling the scale break of convective clouds have not been well studied, it has been reported that cold pools play an important role in increasing the horizontal size of convective clouds. At the boundaries of cold pools, strong convergence due to gust front promotes forced uplifts that are significantly larger than shallow cumulus (Böing et al., 2012). The largest clouds are formed where multiple cold pools collide (Feng et al., 2015). These updrafts with larger radii are less affected by entrainment and eventually become deeper. Recently, Neggers et al. (2019) demonstrated that the maximum size of convective clouds is increased by the mesoscale organization using large-domain LESs and proposed a parameterization using the *org* parameter. Under unorganized conditions, the cloud size is limited by the boundary layer depth since clouds are originated from convective cells in the subcloud layer (Cahalan & Joseph, 1989; Neggers et al., 2003). The mesoscale organized flow can add stochastic variabilities that scale much larger than the boundary layer depth, increasing the size of the largest cloud (e.g., Seifert & Heus, 2013). Still, the physical mechanism of how mesoscale organized flow increases maximum cloud size needs more investigation.

On this basis, we parameterize the scale break radius as a linear function of the mesoscale organization parameter Ω , similar to the parameterization of mean updraft radius in Park (2014):

$$R_b = R_b|_{\Omega=0} + (R_b|_{\Omega=1} - R_b|_{\Omega=0})\Omega, \quad (12)$$

where $R_b|_{\Omega=0}$ and $R_b|_{\Omega=1}$ are R_b at $\Omega = 0$ and $\Omega = 1$, respectively. The parameterization simplifies the mesoscale organization effect on the cloud size limit in an empirical way. Ω is chosen as a proxy for the degree of organization, and a linear relation between Ω and R_b is assumed while other options are available. Nevertheless, Ω , a linear function of the net fractional area of cold pools, is used for the parameterization since a larger area occupied by cold pools indicates an increase in the cold pool boundary and colliding area, increasing the probability of large cloud formation. For simplicity, we assume that correlations between updraft radius and other updraft variables are zero at the near-surface.

2.3. Updraft Sampling Method and a Discussion on Updraft Variabilities

Shin and Park (2020) proposed several methods to sample convective updrafts from the joint PDF at the near-surface. In the proposed methods, an ensemble of updrafts is generated by dividing the joint PDF into a specified number of bins and updrafts are launched with the average values of bins. However, a large number of bins are needed to approximate the true ensemble from the multivariate distribution. Here, “true ensemble” refers to the updraft ensemble in which an infinite number of updrafts are randomly sampled from the joint PDF.

In this study, we use a Monte-Carlo method to sample convective updrafts from the joint PDF. A specified number of updrafts are sampled stochastically from the joint PDF, where the updrafts have equal fractional area. Each sampled updraft has a fractional area of $\hat{a} = \hat{A}_s/n_s$, where \hat{A}_s is the total updraft fractional area at the near-surface and n_s is the number of updrafts to be sampled ($\hat{A}_s = 0.04$ and $n_s = 5$ is used in this study). This method is similar to the sampling strategy used in Sušelj et al. (2013). The sampling method can simulate the ensemble mean of convective tendencies from the true ensemble when averaged for a long time but inevitably

generates large stochastic fluctuation with small n_s . The value of $n_s = 5$ is chosen from the SCM simulations of a tropical convection case with varying n_s . The result of the sensitivity test shows that using a larger number of updrafts (more continuous updraft distribution) reduces the simulated biases and that the simulation results converge at about $n_s > 10$ (Figure S1 in Supporting Information S1). However, the computational time of the convection scheme increases twofold or more at $n_s = 10$. The value of $n_s = 5$ is chosen as a trade-off between the model performance and computational cost.

Physically speaking, cloud variabilities are formed by two stochastic processes, stochastic initialization (at the near-surface or cloud-base height) and stochastic mixing with the environment (Romps & Kuang, 2010). The parameterization of Suselj et al. (2019) is one of the modern stochastic parameterizations built on this physical basis. The scheme uses the near-surface distribution of updrafts and the Poisson distribution of the entrainment rate by assuming that entrainment is a discrete random process. However, previous LES studies have demonstrated that entrainment is highly dependent on cloud and environment properties while it exhibits a considerable amount of stochasticity (Dawe & Austin, 2013; Shin & Baik, 2022). The variabilities of updrafts in stochastic UNICON are formed by the evolution of updrafts which are initialized from the near-surface distribution, where the entrainment and detrainment rates are parameterized as complex functions of updraft properties. More specifically, the mixing between an updraft and the environment is inversely proportional to updraft radius \hat{R} and a buoyancy sorting algorithm determines the entrainment and detrainment rates from the mixed air. The mesoscale organized flow increases the variabilities of updrafts and produces deeper convective clouds by initializing larger updrafts which have reduced entrainment rates. Stochastic UNICON assumes that multiple convective updrafts entrain the same environment properties and that the interaction between plumes occurs only by the mean environment. The heterogeneity of the environment can be neglected for shallow convection (Kurowski et al., 2019). However, the environmental heterogeneity may need to be parameterized for deep convection, especially when convective self-aggregation is presented.

3. Validation of the Framework Using LES Data Sets

In order to validate the assumptions used in the formulation of stochastic UNICON, a series of radiative-convective equilibrium simulations with different radiative cooling rates and vertical shear strengths are conducted with the University of California, Los Angeles large-eddy simulation (UCLA-LES) model (Stevens et al., 1999, 2005). The framework of LES in a radiative-convective equilibrium mode is used to explicitly simulate convection and obtain the statistics of convective updrafts and mesoscale organized flow in near-equilibrium states. Following Cohen and Craig (2006), the radiative forcing is provided as a cooling rate profile, where the cooling rate is constant up to the height of 400 hPa and decreases linearly to 0 between 400 and 200 hPa. A fixed sea surface temperature of 300 K is imposed as a lower boundary condition. For the sheared cases, the mean wind specified in Tompkins (2000) is nudged in a time scale of $\tau = 1$ hr. Four LES configurations with a cooling rate of -2 K day $^{-1}$ or -4 K day $^{-1}$ and with or without wind shear are simulated, denoted as DEEP2K-S, DEEP4K-S, DEEP2K, and DEEP4K.

Two-moment mixed-phase microphysics (Seifert & Beheng, 2006) is used, and surface fluxes are calculated by a similarity theory, where aerodynamic roughness length is obtained from Charnock's relation. The domain size used is $204.8 \times 204.8 \times 26.4$ km 3 , with a horizontal resolution of 200 m and a stretched grid system in the vertical (vertical grid size is 50 m below the height of 1,200 m and increases with a ratio of 0.6% above). To achieve an equilibrium state faster, long-term (3 weeks) simulations with quadrupled grid size are preceded, and then 3 days of high-resolution simulations are initiated with the horizontally averaged profiles at the last time step of the coarser resolution simulations. The model outputs from time intervals of 2 hr during the last 20 hr (10 instantaneous snapshots) are analyzed. The time evolutions of simulated statistics are described in Appendix B. In addition to the deep convection cases, the LES of the BOMEX case is included in this analysis, where the simulation setting is explained in Section 4. The model outputs from time intervals of 1 min during the last 1 hr (60 instantaneous snapshots) are analyzed for the BOMEX LES.

Here, we describe how the convective updraft and cold pool properties are measured in the LES data sets. It is hard to directly measure the statistics of convective updrafts at the near-surface since there is no objective method to define convective updrafts in the subcloud layer. Therefore, we measure the statistics of updraft core properties at the cloud-base height (z_{base}) as a proxy of updraft variabilities in the subcloud layer. This is based on the LES experiment in Shin and Park (2020), which showed that the variabilities of updrafts do not change much in the

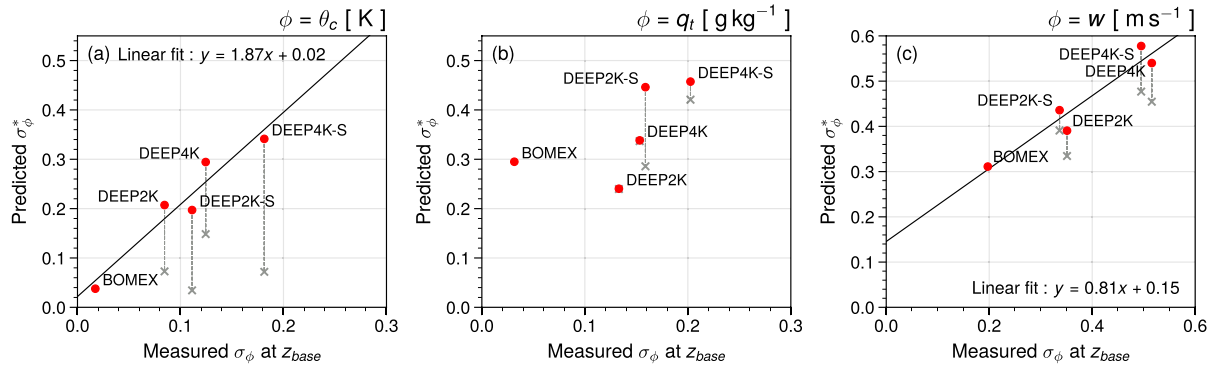


Figure 1. Scatter plots of predicted σ_ϕ^* from Equation 9 versus measured σ_ϕ of updraft cores at the cloud-base height (z_{base}) for (a) $\phi = \theta_c$, (b) $\phi = q_r$, and (c) $\phi = w$ in the five large-eddy simulation cases. The gray cross underneath each red point indicates σ_ϕ^* computed ignoring the effect of mesoscale organization (i.e., $\Delta\phi_\Omega = 0$). In (a and c), linear regression lines and formulas are displayed.

subcloud layer. An updraft core grid is defined as a grid point that has positive buoyancy, nonzero cloud condensate, and positive vertical velocity, and all consecutive core grids are regarded as the same core. For each updraft core, radius ($\sqrt{a/\pi}$, where a is the cross-sectional area) and horizontally-averaged thermodynamic properties are measured. The cold pool air is defined where buoyancy is less than -0.005 m s^{-2} following Tompkins (2001). The net fractional area of cold pools (a_{cp}) is measured as a fraction of the volume occupied by cold pool air below the PBL height, and the mean perturbation of ϕ of cold pools ($\Delta\phi_{\text{cp}}$) is calculated by averaging the anomalies (deviation from grid-mean value) of cold pool air. The PBL height is determined as a height where vertical buoyancy flux is minimum.

First, the parameterization of the distribution of thermodynamic variables is evaluated on how well Equation 9 explains the standard deviations of updraft properties measured in the LES cases. The standard deviations of updraft thermodynamic properties are measured using all updraft cores at the cloud-base height sampled in the LES outputs (“measured σ_ϕ ”). The standard deviations predicted by the parameterization (“predicted σ_ϕ^* ”) are calculated by evaluating Equation 9, where $\Delta\phi_\Omega$ is computed using Equations A2 and A3 with LES-measured cold pool properties (a_{cp} and $\Delta\phi_{\text{cp}}$). c_1 and c_2 in Equation 9 are set to 0.908 and 0.482, respectively, as optimized in Section 5. Figure 1 shows scatter plots of predicted σ_ϕ^* versus measured σ_ϕ of updraft cores at the cloud-base height for $\phi = \theta_c$, q_r , and w . For θ_c and w (Figures 1a and 1c), five LES cases show linear relationships between the two quantities, justifying the parameterization. The updraft variabilities in the DEEP cases are significantly larger than those of the BOMEX case, and the DEEP cases with higher cooling rates show larger variabilities. Particularly, variabilities of $\phi = \theta_c$ are largely increased by mesoscale organized flow, comparing σ_ϕ^* computed with and without the mesoscale organization effect. This is also confirmed in the distribution of θ_c at the near-surface, where the standard deviations of θ_c are much larger than those predicted by the similarity theory (Figure S3 in Supporting Information S1). In contrast to θ_c and w , the data points for $\phi = q_r$ do not show a clear linear relationship (Figure 1b). We suspect that this unexpected result is due to the underestimation of the mesoscale organization effect for q_r . Particularly, $\Delta q_{i,\text{cp}}$ in DEEP2K and DEEP4K are measured values close to zero. The difference between the mean q_i of cold pools and the environment is small since q_i at cold pool center regions is lower than the environment and q_i at cold pool boundaries is higher than the environment (not shown). This is closely related to “water vapor rings” in tropical oceanic cold pools (Langhans & Romps, 2015). Over the ocean, latent heat flux is enhanced in cold pools due to the high near-surface wind speed by density currents, and then the water vapor is transported to the leading edges of cold pools. New convective clouds are triggered by the lifting of relatively moist air at the cold pool boundaries (Feng et al., 2015; Torri et al., 2015). This complex mechanism is not implemented in the current formulation of UNICON, so the moistening of updrafts by the mesoscale organization might be underestimated.

Next, the parameterization of the distribution of the updraft radius is evaluated. Similar to thermodynamic variables, the distribution of updraft core radius is measured at the cloud-base height. Shin and Park (2020) demonstrated that the distribution of the updraft core radius in the BOMEX case is well explained by the proposed parameterization of Equation 11. Figure 2a shows that the distributions of updraft core radius in the DEEP cases also well follow the parameterization with different R_b . The value of R_b for each case is computed by non-linear

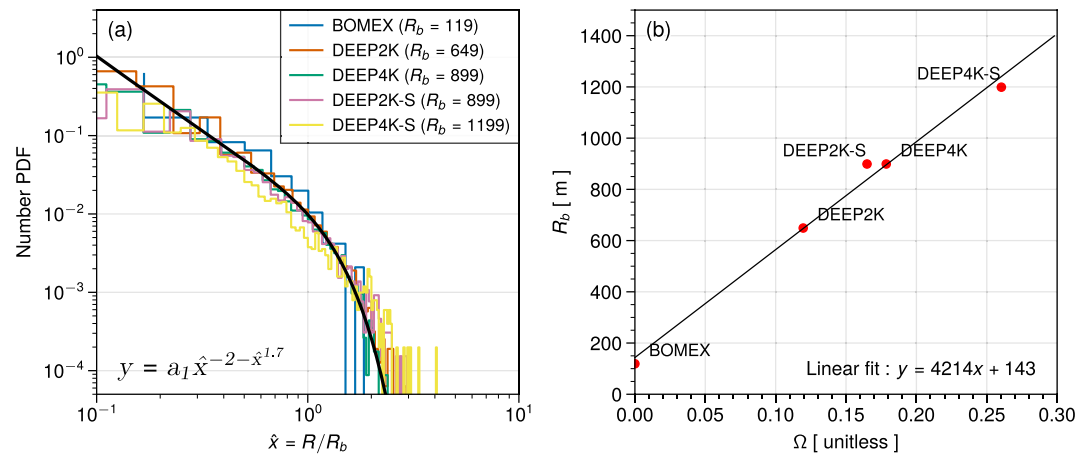


Figure 2. (a) Number PDFs of normalized updraft core radius ($\hat{x} = R/R_b$) measured at the cloud-base height in the five large-eddy simulation (LES) cases. The black line denotes the parameterization of Equation 11. The value of R_b for each case is computed as a non-linear fit to the parameterization in log-log space. (b) Scatter plot of scale break radius R_b versus mesoscale organization parameter Ω measured in the five LES cases and a linear regression line.

fitting of the updraft radius distribution to the parameterization in log-log space. Ω is computed by Equation 1 with the LES-measured a_{cp} . Figure 2b demonstrates that there is a strong linear relationship between R_b and Ω , justifying the parameterization of Equation 12.

4. Single-Column Model Experiment Setup

The SCM used in this study is the single-column version of Community Atmospheric Model version 5 (CAM5). Original UNICON that is identical to the one used by Park et al. (2019) and stochastic UNICON with extension to deep convection are implemented in the model. A series of SCM simulations are performed for 11 different cases over the ocean listed in Table 1 for the optimization of tunable parameters and the evaluation of stochastic UNICON. The listed cases are selected to simulate various cloud types over the ocean. While the development in this study targets deep convection, the cases of shallow convection and stratiform clouds are also included so that the optimization is not biased toward deep convection cases. Land cases are not considered in this study because one of the parameters to be optimized ($R_b|_{\Omega=1}$) is found to be highly dependent on whether the simulation location

Table 1
A List of Single-Column Model Simulation Cases

Name	Long name	Lat	Lon	Start date	Length	Regime	Reference
GATEIII	GATE Phase III	9	336	August 1974	20d	Tropical convection	Houze and Betts (1981)
TOGAII	Tropical Ocean Global Atmosphere	−2	154	December 1992	21d	Tropical convection	Webster and Lukas (1992)
DYNAMO-AMIE	Dynamics of the Madden-Julian Oscillation	−1	73	October 2011	90d	Tropical convection	Yoneyama et al. (2013)
DYNAMO-North	Dynamics of the Madden-Julian Oscillation	3	76	October 2011	90d	Tropical convection	Yoneyama et al. (2013)
DARWIN	Darwin ARM Site	−12	131	November 2004	120d	Tropical convection	May et al. (2008)
BOMEX	Barbados Ocean and Meteorological Experiment	15	300	June 1969	5d (6h)	Shallow convection	Siebesma et al. (2003)
RICO	Rain and Cumulus over Oceans	18	299	December 2004	3d (1d)	Shallow convection	Rauber et al. (2007)
CGILSS6	CFMIP-GASS SCM/LES Intercomparison	17	211	July 1997	30d (10d)	Shallow cumulus	M. Zhang et al. (2013)
CGILSS11	CFMIP-GASS SCM/LES Intercomparison	32	231	July 1997	30d (10d)	Stratocumulus	M. Zhang et al. (2013)
CGILSS12	CFMIP-GASS SCM/LES Intercomparison	35	235	July 1997	30d (10d)	Stratus	M. Zhang et al. (2013)
DYCOMSRF01	Dynamics and Chemistry of Marine StratoCu	32	239	July 2001	2d (4h)	Stratocumulus	Stevens et al. (2005)

Note. The case length in parenthesis denotes the length of LES experiments. GATE = Global Atmospheric Research Program's Atlantic Tropical Experiment, ARM = Atmospheric Radiation Measurement, CFMIP = Cloud Feedback Model Intercomparison Project, GASS = Global Atmospheric System Studies. The DARWIN case is not included in the optimization cases but is used for independent testing.

Table 2
Settings of Idealized Single-Column Model Simulation Cases

Name	Surface flux	Radiation	Geostrophic forcing	Precipitation	N_c [cm ⁻³]
BOMEX	Prescribed	Off	On	Off	–
RICO	Bulk	Off	On	On	70
CGILSS12	Bulk	On	Off	On	100
CGILSS11	Bulk	On	Off	On	100
CGILSS6	Bulk	On	Off	On	100
DYCOMSRF01	Prescribed	On*	On	Off	–

Note. N_c is the specified cloud droplet concentration. RICO and CGILS use simple bulk flux schemes for surface flux calculation. The radiation calculation of DYCOMSRF01 (denoted as *) uses the simplified radiation flux model described in Stevens et al. (2005).

is land or ocean. Therefore, we focus on the simulation of oceanic convection, which has a greater impact on global circulation. The cases can be categorized into two types: time-varying forcing experiments and idealized experiments.

The GATEIII, TOGAIL, DYNAMO-AMIE, DYNAMO-North, and DARWIN cases are time-varying forcing experiments that are simulated with time-varying forcing data collected during intensified observation periods (IOP). The simulated profiles and surface precipitation rates of these cases can be directly compared with observations. The total tendencies of temperature T and moisture q in SCM are calculated by adding large-scale advective tendencies and tendencies from physical processes:

$$\frac{\partial T}{\partial t} = \left(\frac{\partial T}{\partial t} \right)_{\text{xyadv}} + \left(\frac{\partial T}{\partial t} \right)_{\text{zadv}} + \left(\frac{\partial T}{\partial t} \right)_{\text{phys}}, \quad (13)$$

$$\frac{\partial q}{\partial t} = \left(\frac{\partial q}{\partial t} \right)_{\text{xyadv}} + \left(\frac{\partial q}{\partial t} \right)_{\text{zadv}} + \left(\frac{\partial q}{\partial t} \right)_{\text{phys}}. \quad (14)$$

Here, the large-scale advective tendencies are given as

$$\left(\frac{\partial T}{\partial t} \right)_{\text{xyadv}} = -\vec{V} \cdot \nabla T, \quad \left(\frac{\partial T}{\partial t} \right)_{\text{zadv}} = -\omega \frac{\partial T}{\partial p} + \frac{\omega}{c_p} \alpha, \quad (15)$$

$$\left(\frac{\partial q}{\partial t} \right)_{\text{xyadv}} = -\vec{V} \cdot \nabla q, \quad \left(\frac{\partial q}{\partial t} \right)_{\text{zadv}} = -\omega \frac{\partial q}{\partial p}, \quad (16)$$

where \vec{V} is the horizontal wind vector, ω is the vertical pressure velocity, and $\alpha = 1/\rho_{\text{air}}$ is the specific volume of air. The horizontal advective tendencies ($-\vec{V} \cdot \nabla T$, $-\vec{V} \cdot \nabla q$) are prescribed, while the vertical advective tendencies are calculated from prescribed ω and model simulated vertical gradients. To compute the vertical advection from ω , we use a downstream Eulerian difference for temperature and a semi-Lagrangian method for water substances and the other tracers. Sea surface temperature is prescribed so that the surface scheme in CAM5 calculates the surface fluxes. In addition, the observed profiles of horizontal winds are prescribed. The time-varying forcing experiments are conducted with 30 vertical levels and a model time step of $\Delta t = 1,200$ s. The DARWIN case originally spans more than 5 months, from 3 November 2004 to 29 April 2005. However, the forcing for this site is not continuous and broken into 11 segments, so we choose the longest continuous segment.

The BOMEX, RICO, CGILSS12, CGILSS11, CGILSS6, and DYCOMSRF01 cases are idealized experiments that produce near-equilibrium states with idealized (or time-averaged) forcings. These cases are designed to conduct LES intercomparison experiments in controlled environments. For these cases, we simulate the SCM with the same settings and forcings as the LES to compare with the LES results. The settings of the cases are summarized in Table 2, and detailed settings are available in their companion LES intercomparison studies (BOMEX: Siebesma et al. (2003); RICO: vanZanten et al. (2011); CGILS: Blossey et al. (2013), DYCOMSRF01: Stevens et al. (2005)). In BOMEX and RICO, radiation schemes are disabled; instead, radiative cooling tendencies are specified. The cloud droplet concentration is specified for RICO, but it does not affect the SCM simulation because

UNICON uses simple single-moment microphysics. The idealized experiments are conducted with 80 vertical levels and a model time step of $\Delta t = 300$ s. More vertical levels (80 levels) are used compared to time-varying forcing experiments (30 levels) since turbulence and clouds are concentrated in the lower troposphere.

For the idealized experiments, LES model outputs are considered observations. We use publicly available LES model outputs of LES intercomparison studies for the DYCOMSRF01 (12 models) and CGILS (6 models) cases. For the BOMEX and RICO cases, we simulate those with UCLA-LES with the settings of Siebesma et al. (2003) and vanZanten et al. (2011), respectively. The only difference with these intercomparison studies is that we use smaller grid sizes of $25 \times 25 \times 25$ m³ and $40 \times 40 \times 40$ m³ for the BOMEX and RICO cases, respectively (domain sizes are $6.4 \times 6.4 \times 3.0$ km³ and $12.8 \times 12.8 \times 4.0$ km³, respectively).

5. Optimization

5.1. Optimization Strategy

Undetermined parameters in stochastic UNICON are optimized using multiple SCM cases to increase the accuracy of simulations under various large-scale environments. Ten SCM cases, except the DARWIN case, are used for the optimization, while the DARWIN case is used for an independent test. The relatively long observation period of the DARWIN case (120 days) provides sufficient time length for the independent test. The following four parameters of stochastic UNICON are subject to optimization: $R_b|_{\Omega=0}$, $R_b|_{\Omega=1}$, c_1 , and c_2 .

Here, we describe the variables that are selected for model evaluation in the optimization process. It is a common practice to use large-scale atmospheric variables for model calibration, which are u , v , ω , T , q , surface pressure, total precipitation rate, and outgoing radiative fluxes (e.g., Dunbar et al., 2021; Neelin et al., 2010; T. Zhang et al., 2015), so we consider these variables. The design of the SCM experiment constrains the selection since u , v , ω , and surface pressure are prescribed as observations. The observations on radiative fluxes are only available in the DYNAMO and DARWIN cases. Therefore, we choose moist static energy ($MSE = c_p T + gz + L_v q_v$, where g is the gravitational acceleration and q_v is the water vapor specific humidity) and surface precipitation rate to evaluate model performance. The moist static energy is chosen because it contains information about both temperature and moisture and is a good diagnostic variable for convective transport. For the optimization of a convection parameterization, it may be ideal to include variables directly associated with convection and clouds in the cost function, such as cloud fraction and liquid/ice water content. If a model optimization is targeted to reduce errors of large-scale atmospheric variables only, then there is a possibility that the optimized model deteriorates the simulation of convection and clouds while the errors in large-scale atmospheric variables are reduced. Therefore, a more objective method of calibrating model parameters to improve model behavior at the process level needs to be developed. One option is to generate an ensemble of cloud-resolving simulations and design a target metric based on the simulated cloud properties (e.g., Hourdin et al., 2021).

The standard approach to dealing with optimization problems that involve multiple cases or variables is multiobjective optimization (Deb, 2014; Neelin et al., 2010). In multiobjective optimization, objective functions of different variables are lumped into a single weighted cost function. Typically, the weighted cost function is defined as $J = \sum_k w_k f_k$, where w_k is the weight and f_k is the objective function such as the square error or root-mean-squared error (RMSE). The selection of w_k is arbitrary because it depends on how a particular user evaluates accuracy in certain cases or certain variables.

Using the multiobjective approach with equal weights for the cases and variables, we define the cost function for our optimization problem as

$$J = \frac{1}{N_{case}} \sum_{k=1}^{N_{case}} \left[\frac{1}{2} \cdot \text{RMSE}^*(\text{MSE}_k) + \frac{1}{2} \cdot \text{RMSE}^*(\text{PREC}_k) \right], \quad (17)$$

$$\text{RMSE}^*(\phi_k) = \frac{\text{RMSE}(\phi_{k,\text{UNICON-STO}})}{\text{RMSE}(\phi_{k,\text{UNICON}})}, \quad (18)$$

where $N_{case} = 10$ is the number of SCM cases, MSE_k and PREC_k are the moist static energy and surface precipitation rate of each case, respectively, and RMSE^* is the relative RMSE where the RMSE of stochastic UNICON is divided by the RMSE of original UNICON. By normalizing RMSE by that of the control simulation, the objective function of each variable is non-dimensionalized and the cost function becomes an improvement index

where the value smaller than one indicates better performance than the control simulation. The design of the cost function is identical to that used in T. Zhang et al. (2015).

Before calculating the RMSE of moist static energy, simulated moist static energy is interpolated into the vertical levels of observations (IOP observations for the time-varying forcing cases and LES for the idealized cases). Precipitation rates are 12-hr running averaged to remove high-frequency noise due to the Monte-Carlo sampling method of stochastic UNICON. Finally, RMSEs are calculated using all time steps and entire vertical levels during the case period. We calculate the RMSEs of precipitation rates only for the time-varying forcing cases. The idealized cases are boundary-layer cloud cases which produce significantly lower precipitation rates than deep convection cases. Also, the LES intercomparison results of RICO and CGILS (only CGILSS6 produces non-negligible precipitation) show very different precipitation rates among LES models (Blossey et al., 2013; vanZanten et al., 2011). For these reasons, $\text{RMSE}^*(\text{PREC}_k)$ is set to 1 for the idealized SCM cases.

We use Bayesian optimization method to search a global minimum of cost function J . Bayesian optimization is suitable when the objective function $f(x)$ (where x is a vector of parameters) is expensive to evaluate and the gradient of $f(x)$ is unavailable, so an optimization based on gradient descent is not feasible. The Bayesian optimization also tolerates stochastic noise in $f(x)$ and quantifies the uncertainty. The Bayesian optimization consists of a surrogate model and an acquisition function. The surrogate model estimates the distribution of the function $f(x)$ based on the previously evaluated points $((x_1, f(x_1)), (x_2, f(x_2)), \dots, (x_n, f(x_n)))$ using Gaussian process regression (Rasmussen, 2003). The acquisition function suggests next evaluation point that minimizes the function $f(x)$ based on the results of the surrogate model. The process is repeated for a fixed number of iterations, and evaluation points consequently approach to global minimum of $f(x)$.

The search space for the parameters is set as $R_b|_{\Omega=0} = [50, 500]$, $R_b|_{\Omega=1} = [1,000, 5,000]$, $c_1 = [0.1, 1.0]$, and $c_2 = [0.1, 1.5]$. The search space is determined sufficiently broadly in consideration of physically possible range of each parameter. Before optimization, we evaluate 200 initial points selected by Latin hypercube sampling (McKay et al., 1979) in the search space. Finally, the Bayesian optimization is conducted with 800 iterations, using expected improvement (Jones et al., 1998) as the acquisition function. The optimized value x_{opt} is defined where the posterior mean of the Gaussian process is minimum because our cost function J includes a substantial amount of stochasticity. The optimization is done with a Python Bayesian optimization library, GPyOpt (González et al., 2016).

Here, we discuss a potential issue according to the design of optimization. There is a possibility that the improvement in the tropical convection cases simulated by the optimized stochastic UNICON is trivial because the cost function is designed to reduce the RMSE of moist static energy at each vertical level. The improvement is “meaningful” when physical processes are improved without inconsistency and when the improvement is general for various circumstances. In this study, we use several strategies to make sure that the improvement by the optimization is physically meaningful and generalizable. The shallow convection and stratiform cloud cases are included in the optimization so that the physical processes other than deep convection do not deteriorate. An independent case (DARWIN), which is not included in the optimization, is evaluated to determine whether the optimization is biased toward the trained cases. Finally, the simulated cloud statistics are evaluated using the LES results for the idealized SCM cases (e.g., Figures 12 and 13). However, the simulated statistics of convective clouds in the tropical convection cases are not evaluated in this study due to the lack of observations. A better optimization design would be using a larger set of observational data and a process-level calibration which uses a target metric based on process-level statistics.

5.2. Optimization Results

The optimized values of the parameters x_{opt} are $R_b|_{\Omega=0} = 108$ m, $R_b|_{\Omega=1} = 2,190$ m, $c_1 = 0.908$, and $c_2 = 0.482$ (Table 3). After about 400 iterations, the result of the optimization is converged. The first row of Figure 3 shows all evaluation points during the Bayesian optimization. Some of the evaluation points have cost functions greater than 1, where stochastic UNICON performs worse than original UNICON. Most evaluation points have cost functions smaller than 0.95. The posterior mean of the Gaussian process at x_{opt} is measured as 0.893, and the cost function evaluated at x_{opt} is 0.885.

We can roughly see parameter sensitivity from each of Figures 3a–3d (i.e., smaller cost functions near the optimized value), but it is not clear since the evaluation points in the 4-dimensional parameter space are projected

Table 3
Optimized Parameters in Stochastic UNICON

Parameter	Search range	Optimized value	Description
$R_b _{\Omega=0}$	50–500	108 m	Scale break radius at the near-surface at $\Omega = 0$ (Equation 12)
$R_b _{\Omega=1}$	1,000–5,000	2,190 m	Scale break radius at the near-surface at $\Omega = 1$ (Equation 12)
c_1	0.1–1.0	0.908	Scaling factor for variance from non-organized turbulence (Equation 9)
c_2	0.1–1.5	0.482	Scaling factor for variance from mesoscale organized flow (Equation 9)

to single parameter space. In order to visualize the parameter sensitivity, a single-parameter sensitivity test is conducted. The test varies a single parameter while fixing other parameters as the optimized values. For each parameter, 100 points equally spaced within the search space of the parameter are evaluated. The sensitivity test shows that all four parameters have considerable impacts on the performance of stochastic UNICON (second row of Figure 3). Roughly, the Bayesian optimization seems to approach true optimum. However, in the case of $R_b|_{\Omega=1}$, smallest cost functions are observed near 3,000 m. This value is larger than the optimized value (Figure 3f). The Bayesian optimization can underperform when the noise level is high in objective functions (Letham et al., 2019). One possible solution is to perform multiple ensemble simulations for each case to reduce variance in the cost function.

The first row of Table 4 summarizes the relative RMSEs of moist static energy and surface precipitation rate simulated by stochastic UNICON with the optimized parameters. Optimized stochastic UNICON outperforms original UNICON in most cases. The improvement is apparent for the thermodynamic profiles of tropical convection cases, where RMSEs in moist static energy are reduced by 21–45%. The precipitation rates are also significantly improved in stochastic UNICON except in the GATEIII case. For the idealized cases, the significant reduction of RMSE is only notable in the BOMEX case. The performances of original UNICON and stochastic UNICON are almost identical for the DYCOMSRF01 case. The detailed single-column simulation results of optimized stochastic UNICON are described in Section 6.

In addition to new stochastic UNICON, we evaluate the model performances of two different versions of stochastic UNICON to demonstrate the impact of the mesoscale organization effects. One is the previous version of stochastic UNICON by Shin and Park (2020) (old stochastic UNICON hereinafter; second row of Table 4), and the other is the old stochastic UNICON with the organization effect on updraft radius as parameterized as Equation 12 (third row of Table 4). New stochastic UNICON can be thought of as old stochastic UNICON with the organization effects both on updraft radius and thermodynamic variables. For consistency, the optimized parameter values in Table 3 are used for all versions of stochastic UNICON. The three versions are exactly the same

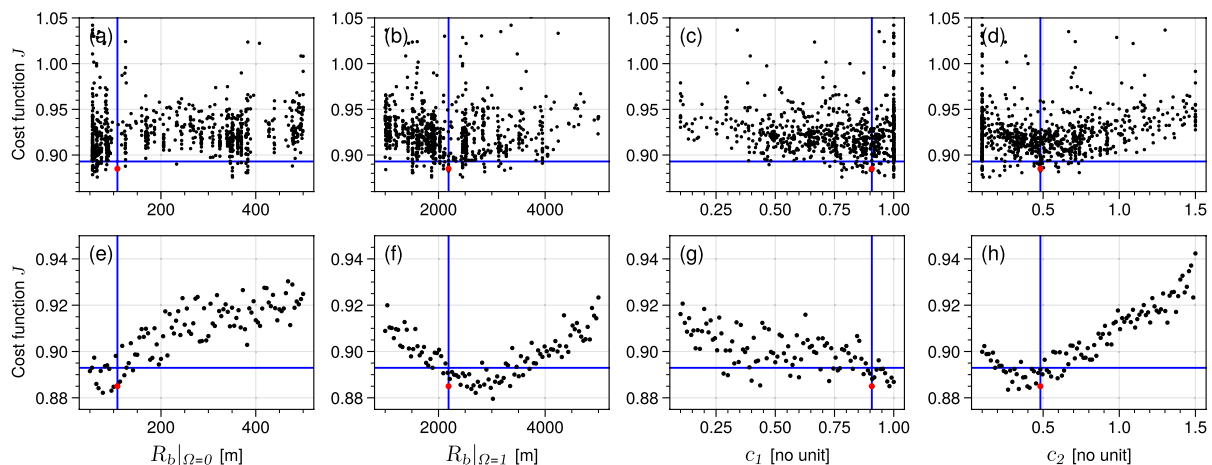


Figure 3. (a–d) Scatter plots of the evaluation points during the Bayesian optimization. (e–h) Scatter plots of the evaluation points of the single-parameter sensitivity test, which varies a single parameter while fixing other parameters as the optimized values. Vertical blue lines denote the optimized parameters x_{opt} where the posterior mean of the Gaussian process is minimum. Horizontal blue lines denote the minimum value of the posterior mean at x_{opt} ($J = 0.893$). Red dots denote the cost function evaluated at x_{opt} ($J = 0.885$).

Table 4
Relative RMSEs (RMSE(UNICON-STO)/RMSE(UNICON)) of Moist Static Energy and Surface Precipitation Rate Simulated by (First Row) New Stochastic UNICON, (Second Row) the Old Version of Stochastic UNICON by Shin and Park (2020), and (Third Row) the Old Stochastic UNICON With Organization Effect on Updraft Radius

		TOGAII	GATEIII	DYNAMO-AMIE	DYNAMO-North	DARWIN	BOMEX	RICO	CGILSS6	CGILSS11	CGILSS12	DYCOMSRF01
New UNICON-STO	MSE	0.780	0.788	0.547	0.588	0.759	0.718	0.971	0.957	0.981	0.959	1.000
	PREC	0.869	1.003	0.789	0.748	0.699	—	—	—	—	—	—
Old UNICON-STO	MSE	1.512	1.628	1.977	1.980	3.443	0.718	0.976	0.957	0.981	0.959	1.000
	PREC	1.269	1.312	1.138	1.113	1.423	—	—	—	—	—	—
Old UNICON-STO (+ organization effect on radius)	MSE	1.008	0.954	0.650	0.773	0.893	0.718	0.976	0.957	0.981	0.959	1.000
	PREC	0.882	0.957	0.746	0.725	0.757	—	—	—	—	—	—

Note. The optimized parameters in Table 3 are identically used for the three versions of stochastic UNICON.

when the mesoscale organization is absent, so the simulation results are identical for the idealized cases other than RICO. The RMSEs of the RICO case show only slight differences among the scheme versions due to weak mesoscale organization. Old stochastic UNICON shows substantially worse performances than the original UNICON (relative RMSEs greater than 1) for the tropical convection cases because old stochastic UNICON does not simulate organized convection at all. The old stochastic UNICON with the organization effect on updraft radius shows performances in between the original UNICON and new stochastic UNICON for the tropical convection cases. The inclusion of the organization effect on updraft radius considerably increases model performance by simulating large updrafts when the mesoscale organization is presented. Still, the best performance is achieved when the organization effects on both updraft radius and thermodynamic variables are included (new stochastic UNICON). The result suggests that both the stochastic impacts of non-organized turbulence and mesoscale organization contribute to the performance improvement in stochastic UNICON.

6. Single-Column Model Simulation Results

6.1. Time-Varying Forcing Experiments

Table 5 summarizes the RMSEs of temperature, specific humidity, moist static energy, and precipitation simulated by UNICON and stochastic UNICON for the time-varying forcing SCM cases. Stochastic UNICON displays consistently lower RMSEs than UNICON for all variables except precipitation in the GATE case. The reduction of RMSEs of moist static energy by stochastic UNICON is both contributed by the decrease in RMSEs of temperature and specific humidity. Vertical profiles of the simulated biases in these SCM cases (Figures 4 and 5; Figures S4, S5, and S6 in Supporting Information S1) demonstrate that stochastic UNICON reduces the persistent biases in UNICON, which are characterized by negative temperature bias in the upper troposphere and dry bias in the lower troposphere. The DARWIN case, which is not included in the optimization, also shows considerable performance improvement by stochastic UNICON with optimized parameters (Figure S6 in Supporting Information S1). The result suggests that the parameters are less likely to be overfitted to the cases subject to optimization. To get more insights into the characteristics of the simulation of stochastic UNICON, we will discuss in detail the simulation results of the TOGAII and DYNAMO-AMIE cases.

The TOGAII case's IOP took place in the western Pacific warm pool region, and the SCM simulation results of 21 days starting from 18 December 1992 are shown in Figure 4. Two groups of rainfall events are observed during 18–29 December and 1–7 January (Figure 4a). Most of the rainfall during these periods is from mesoscale convective system (MCS) scale squall lines (Rickenbach & Rutledge, 1998). The first group of rainfall events is associated with a prominent MJO event, which started in early December and decayed during the end of December (Lin & Johnson, 1996). Both UNICON and stochastic UNICON skillfully predict approximate variations of observed precipitation rates. However, UNICON overestimated the intensities of rainfall peaks on 19 December, 26 December, and 1 January, which increases the RMSE of UNICON. The negative temperature biases above 500 hPa level in UNICON are reduced in stochastic UNICON. However, stochastic UNICON shows a stronger negative temperature bias centered at 300 hPa level on 2 January. The negative temperature bias is due to the lack of heat source during the very end of December. This period is a decaying period of the MJO when the fraction of stratiform precipitation from anvil clouds is high (Johnson et al., 2016). Johnson et al. (2016) showed that the apparent heat source (Q_1) in the upper troposphere is highest when the fraction of stratiform precipitation is high, using radar data during TOGA. The intense heating effect of anvil stratiform precipitation is due to its large cover and association with the freezing of hydrometeors (0°C level is about 650 hPa level). UNICON produces strong convection on 1 January, which reduces the negative temperature bias in the upper troposphere, but it seems unrealistic, as seen from the overestimated rain peak on 1 January. These results suggest that UNICON and stochastic UNICON do not realistically simulate anvil clouds and their impacts with the current formulation. The negative humidity bias of original UNICON is reduced in stochastic UNICON, but the relatively weak positive humidity bias is produced in stochastic UNICON during December. The negative moist static energy bias is reduced in stochastic UNICON, with positive biases in the lower troposphere and negative biases in the upper troposphere.

Table 5

RMSEs (in the Form of $RMSE(UNICON-STO)/RMSE(UNICON)$) of Temperature, Specific Humidity, Moist Static Energy, and Surface Precipitation Rate Simulated by Stochastic UNICON and Original UNICON for the Time-Varying Forcing Single-Column Model Cases

	TOGAII	GATEIII	DYNAMO-AMIE	DYNAMO-North	DARWIN
T (K)	2.409/2.770 (−13.0%)	1.645/1.794 (−8.3%)	2.646/3.492 (−24.2%)	3.203/4.408 (−27.3%)	3.191/3.659 (−12.8%)
q (g kg ^{−1})	0.574/0.785 (−26.9%)	0.455/0.767 (−40.6%)	0.623/1.316 (−52.7%)	0.928/1.726 (−46.2%)	1.101/1.818 (−39.4%)
MSE (kJ)	3.094/3.969 (−22.0%)	2.131/2.706 (−21.2%)	3.099/5.666 (−45.3%)	4.541/7.727 (−41.2%)	4.076/5.366 (−24.1%)
PREC (mm day ^{−1})	3.870/4.452 (−13.1%)	4.768/4.754 (0.3%)	3.378/4.281 (−21.1%)	3.090/4.131 (−25.2%)	4.344/6.216 (−30.1%)

Note. The rate of change in RMSE is denoted in parenthesis.

The DYNAMO-AMIE case is part of the Dynamics of the Madden-Julian Oscillation (DYNAMO) field campaign and the ARM Madden-Julian Oscillation Investigation Experiment (AMIE) field campaign, where the forcing data were collected from Gan island on Addu Atoll for 90 days beginning on 1 October 2011 (Figure 5). This case shows the life cycles of the MJO and the associated developing and decaying of convective systems over the Indian Ocean. During DYNAMO-AMIE, three large-scale convective events (LCEs) are observed, which are referred to as LCE1, LCE2, and LCE3 following Powell and Houze (2013). LCE1 and LCE2 are associated with robust MJO events, and multiple large MCSs were observed by the radar system on Addu Atoll during these periods (Powell & Houze, 2013). LCE3 is associated with a less prominent MJO event, and an isolated MCS and several squall lines were observed during the period. The MJO phase calculated by the method of Wheeler and Hendon (2004) provides a broad-scale view of the phase of convection activity over the tropical Indo-Pacific (Figure 5a). At the DYNAMO-AMIE location, phases 8–3 correspond to active convection MJO phases and phases 4–7 are inactive MJO phases. The precipitation enhancements during LCE1 and LCE2 are consistent with active MJO phases. However, the LCE3 period corresponds to phases 4 and 5 which are inactive MJO phases. The detailed analysis of the simulations depending on MJO phases will be discussed in Section 6.2.

Stochastic UNICON shows the RMSE of simulated precipitation that is 21% less than UNICON. UNICON produces a number of rain peaks with erroneously estimated intensity, especially during the decaying stage of MJO events (Figure 5a). The overestimated rain peaks are produced from late November to early December (the last part of LCE2). UNICON displays continuous strong negative temperature biases in the upper troposphere, and the bias is strongest during this period (Figure 5b). Due to the bias, UNICON produces unrealistically strong convection to stabilize the atmosphere, as in the TOGAII case. UNICON also shows negative humidity and moist static energy biases. Stochastic UNICON significantly reduces the temperature, humidity, and moist static energy biases. Still, stochastic UNICON displays a negative upper-level temperature bias, especially during the MJO decaying periods, implying that the diabatic heating from anvil clouds and stratiform precipitation system is underestimated.

To better understand the simulation results, time-averaged vertical profiles of convective mass fluxes and tendencies due to convection and PBL schemes are drawn (Figure 6). The plotted tendencies include tendencies from turbulent mixing and convection microphysics but do not include tendencies from stratiform microphysics and radiation. Among the five cases, stochastic UNICON produces stronger updraft mass fluxes below 500 hPa level and slightly weaker mass fluxes at upper levels, compared to UNICON. This is because stochastic UNICON launches a spectrum of multiple updrafts, so less buoyant updrafts are detrained into the environment at lower levels. The downdraft mass flux in stochastic UNICON is also larger at lower levels since downdrafts are generated from negatively buoyant detrained air.

Stochastic UNICON shows higher heating tendencies by convection compared to UNICON, considering that the tendencies due to the PBL scheme are limited in the boundary layer (second row of Figure 6). This enhanced convective heating contributes to reducing the negative temperature biases presented by UNICON. In the specific humidity tendencies, stochastic UNICON displays higher drying tendencies by convection in the mid-troposphere. This seems to be contrary to the result that stochastic UNICON reduces dry biases of UNICON. In fact, the higher drying tendency in the mid-troposphere contributes to reducing the dry bias because it increases the vertical gradient of specific humidity, so the specific humidity tendency due to vertical advection ($-\omega\partial q/\partial p$) is increased. This will be discussed in detail in Section 6.2.

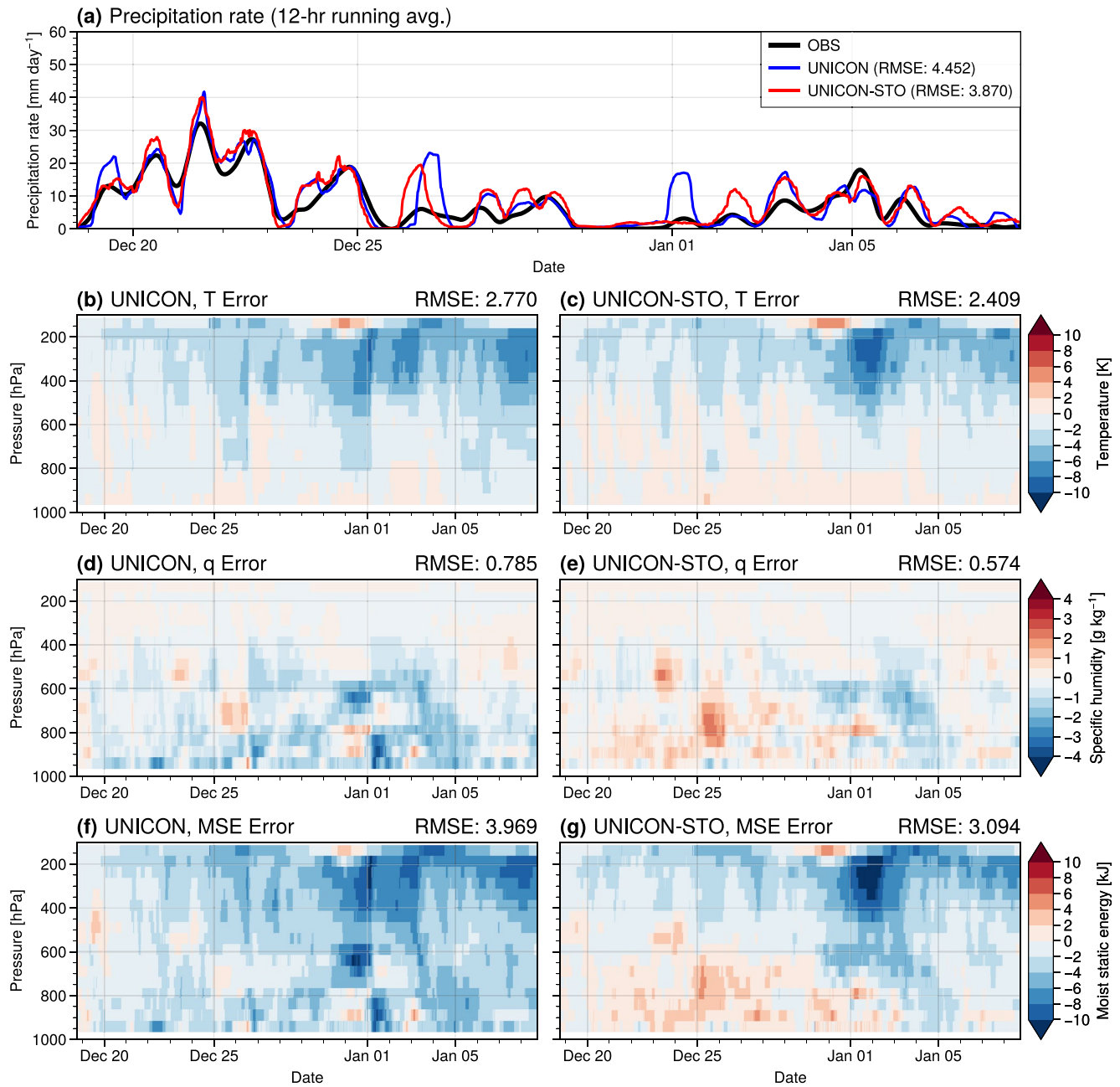


Figure 4. (a) Time series of surface precipitation rates from IOP observation and UNICON and UNICON-STO simulations in the TOGAII case. The time series are smoothed with 12-hr running averages. (b–g) Errors of temperature, specific humidity, and moist static energy simulated by UNICON and UNICON-STO, with respect to observation, in the TOGAII case. Root mean squared errors are given at the upper right of each plot.

Figure 7 shows temperature and specific humidity tendencies separated by detailed convective processes in the DYNAMO-AMIE case. The convective updrafts generate heating tendency (drying tendency) mostly by the production of convective precipitation, and convective downdrafts generate cooling tendency (moistening tendency) mostly by evaporation of convective precipitation. The increased heating and drying tendencies of stochastic UNICON are contributed both by convective updrafts and downdrafts, where convective updrafts contribute below 500 hPa level and convective downdrafts contribute above 500 hPa level.

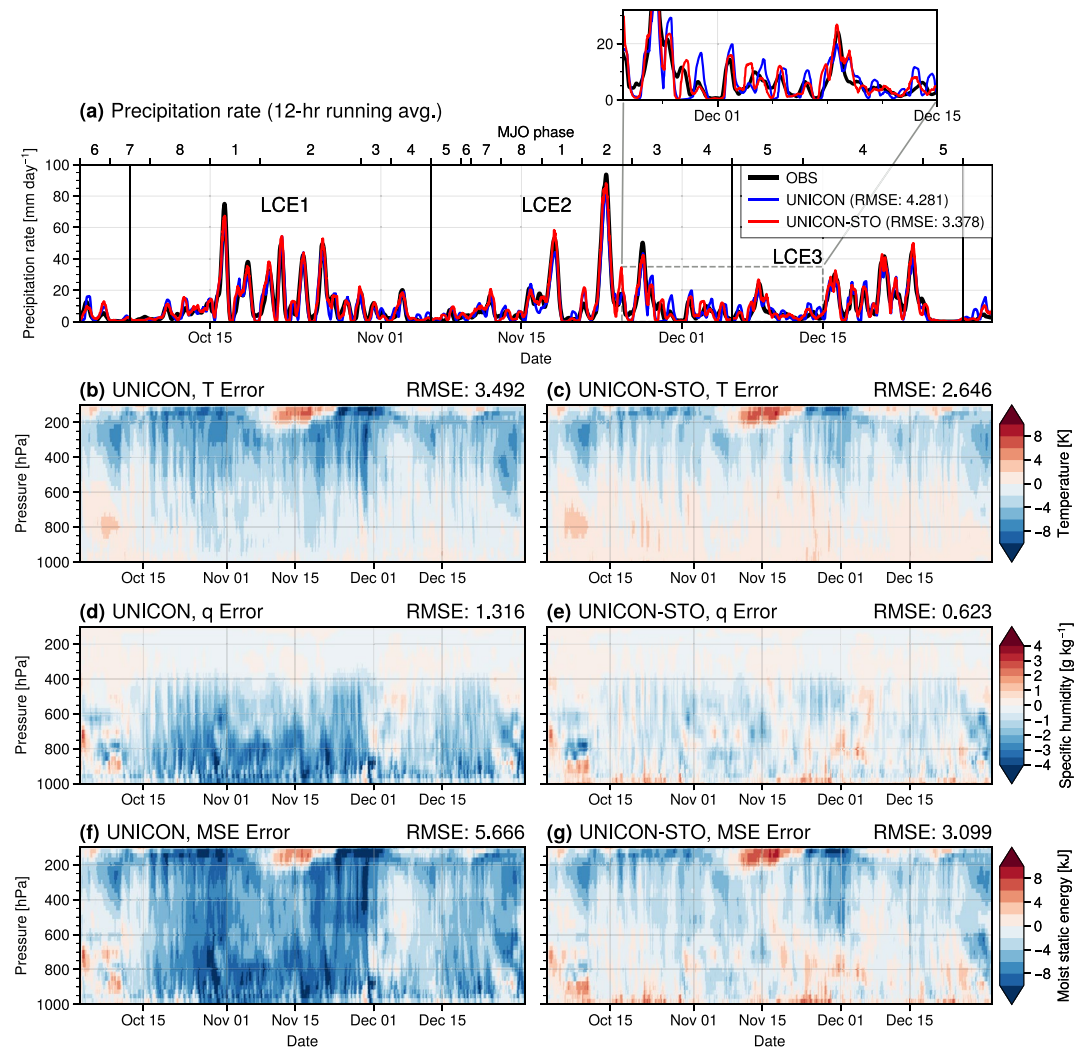


Figure 5. (a) Time series of surface precipitation rates from IOP observation and UNICON and UNICON-STO simulations in the DYNAMO-AMIE case. The time series are smoothed with 12-hr running averages. Wheeler and Hendon (2004) Madden-Julian oscillation phases are denoted along the top axis. Durations of three large-scale convective events (LCEs) are denoted with black vertical lines. (b–g) Errors of temperature, specific humidity, and moist static energy simulated by UNICON and UNICON-STO, with respect to observation, in the DYNAMO-AMIE case. Root mean squared errors are given at the upper right of each plot.

6.2. Simulated MJO in the DYNAMO-AMIE Case

In this subsection, the characteristics of simulated MJO in the DYNAMO-AMIE case are analyzed in detail. Figure 8 shows smoothed anomalies of temperature (T'), specific humidity (q'), and moist static energy (MSE') in the DYNAMO-AMIE case. In observation, slight positive anomalies in temperature in the upper troposphere are concurrent with positive moisture anomalies for each LCE when convection activities are high (Figures 8a and 8d). It is observed that the heights of positive moisture anomalies increase as time progresses during each LCE. At the early stages of LCEs, strong moistening begins between 850 and 700 hPa after dry anomalies. The positive moisture anomalies are vertically extended as convection activities increase. Stochastic UNICON successfully captures the positive temperature and moisture anomalies during the active convection periods and the progressively increasing heights of positive moisture anomalies. However, stochastic UNICON overestimates the magnitude of temperature anomalies at the upper levels (Figure 8c). Original UNICON does not correctly capture the oscillation of temperature and moisture anomalies, and the simulated positive anomalies during LCE2 are indistinct. In addition, too strong positive temperature anomalies are generated at the beginning of LCE1 and LCE3. The intense heating tendency at the end of LCE2 indicates that unrealistically strong convection is

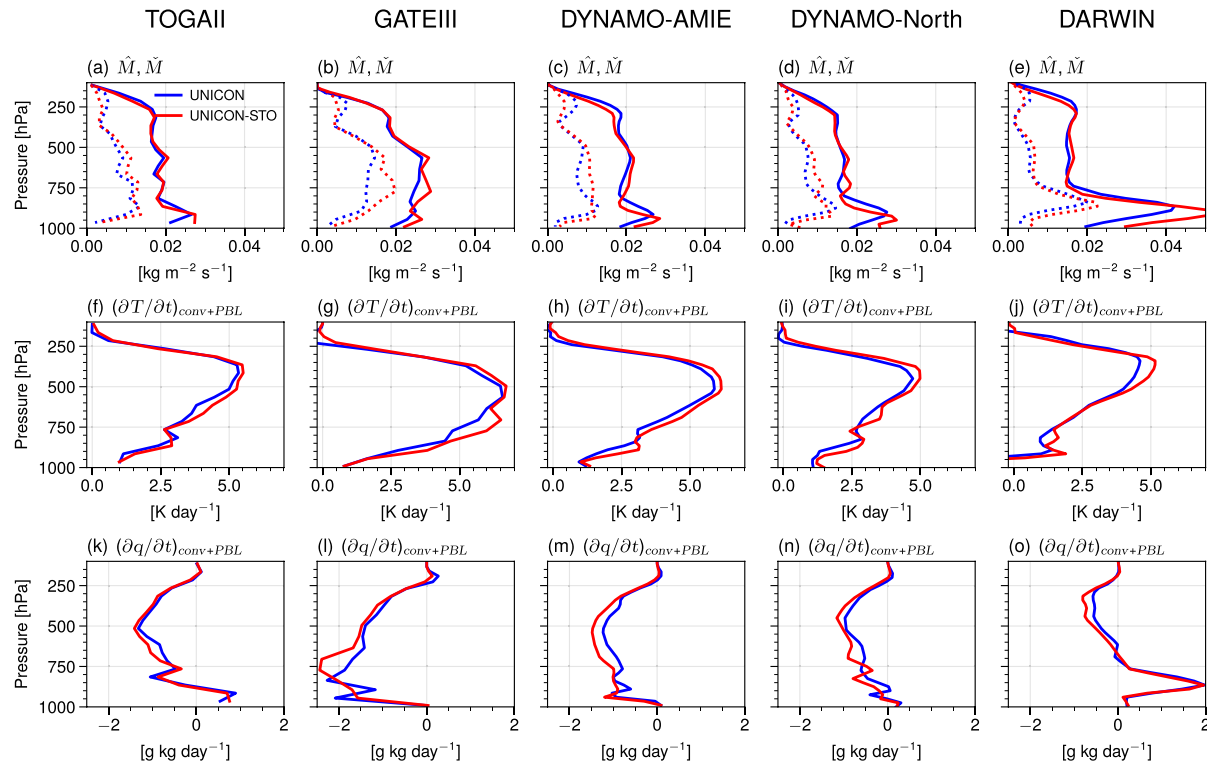


Figure 6. Vertical profiles of time-averaged (a–d) convective updraft mass flux (\hat{M} , solid lines) and downdraft mass flux (\tilde{M} , dashed lines), (e–h) temperature tendency by convection and planetary boundary layer (PBL) schemes, and (i–l) specific humidity tendency by convection and PBL schemes simulated by UNICON and stochastic UNICON in the time-varying forcing single-column model cases.

simulated, which produces overestimated rain peaks during this period (Figure 5a). The results here suggest that stochastic UNICON can improve the MJO simulation by representing a more realistic interaction between large-scale forcings and convection.

Figure 9 shows vertical profiles of relative humidity, updraft mass flux, and normalized probability of convection top composited by the active MJO phases (phases 8–3) and inactive MJO phases (phases 4–7). The observed relative humidity is significantly higher during the active MJO phases than during the inactive MJO phases throughout the troposphere (Figure 9a). The environment with higher relative humidity promotes deeper

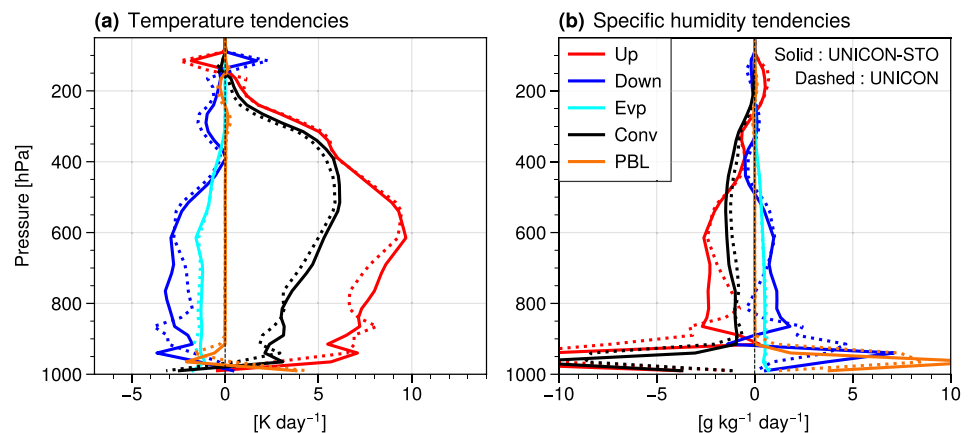


Figure 7. Vertical profiles of time-averaged (a) temperature and (b) specific humidity tendencies by convective updrafts (Up), convective downdrafts (Down), evaporation of convective precipitation within the environment (Evp), total convective processes (Conv), and the planetary boundary layer (PBL) scheme (PBL) simulated by UNICON and stochastic UNICON in the DYNAMO-AMIE case. Solid lines denote stochastic UNICON, and dashed lines denote UNICON.

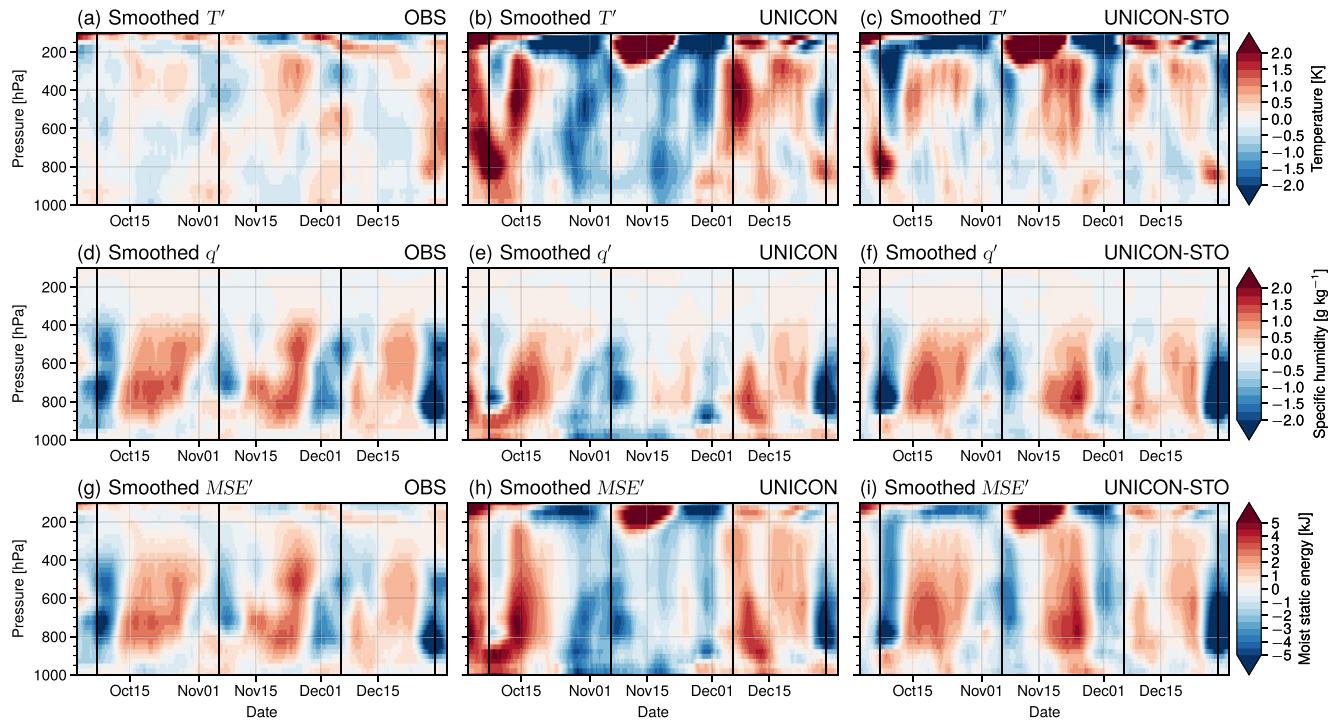


Figure 8. Smoothed anomalies of (a–c) temperature (T'), (d–f) specific humidity (q'), and (g–i) moist static energy (MSE') from observation, UNICON, and UNICON-STO in the DYNAMO-AMIE case. All anomalies are calculated relative to the mean value of the entire period and smoothed by 5-day running averages. Durations of three large-scale convective events (LCEs) are denoted with black vertical lines.

convection by reducing the dilution of convective updrafts by mixing. The simulated relative humidity profiles also display dependency on MJO phases. However, UNICON and stochastic UNICON simulate lower relative humidity below the 450 hPa level and higher relative humidity above compared to observation. Notably, the relative humidity close to 100% at heights above 300 hPa indicates the excessive amount of high-level clouds in the SCM simulations. Stochastic UNICON reduces the relative humidity bias of UNICON below 600 hPa level. The simulated updraft mass flux above 850 hPa level during the active MJO phases is much higher than that during the inactive MJO phases (Figure 9b). It is notable that the updraft mass fluxes at the near-surface do not change much along with MJO phases, implying that the variation of convection activity associated with the

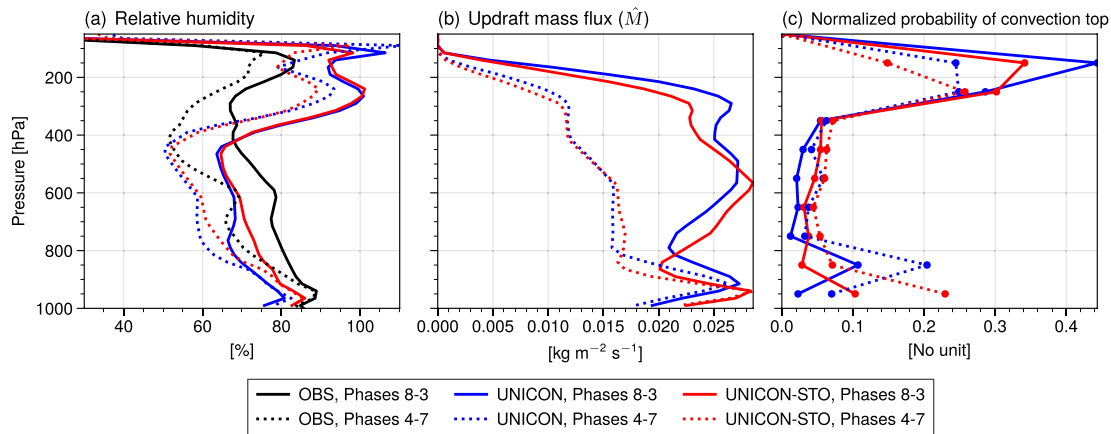


Figure 9. Vertical profiles of time-averaged (a) relative humidity, (b) updraft mass flux, (c) normalized probability of convection top during Madden-Julian oscillation phases 8-3 and phases 4-7 in the DYNAMO-AMIE case, simulated by UNICON and UNICON-STO. For relative humidity, profiles from observation are also shown. The normalized probability of convection top is calculated by accumulating the fractional area of saturated updraft top in each 100 hPa bin and then normalizing by the total sum of the bins.

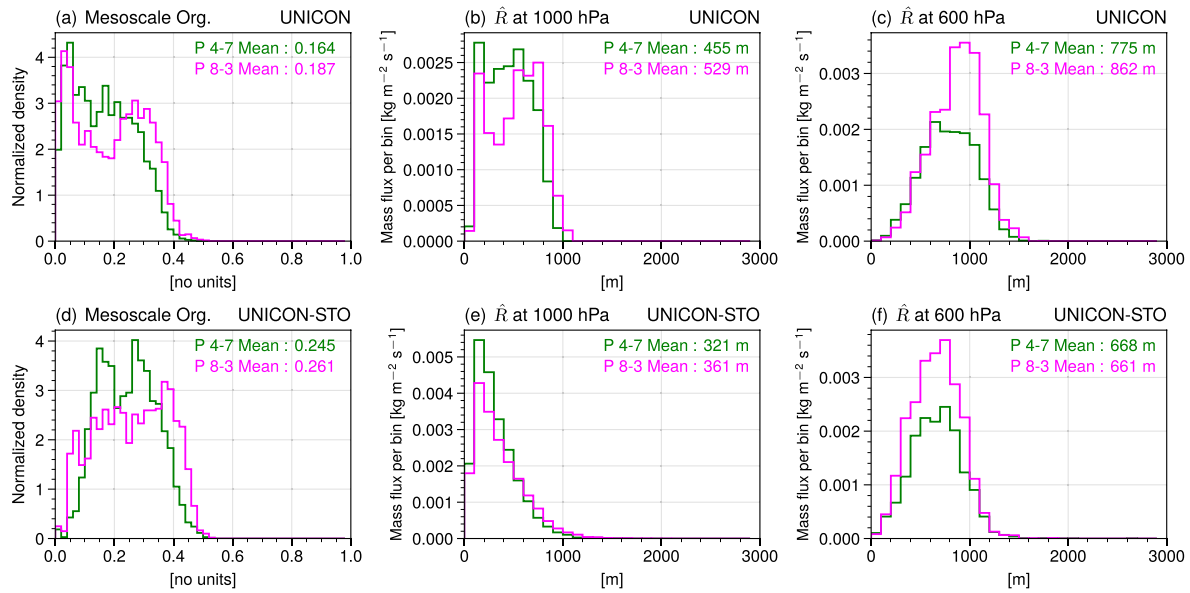


Figure 10. (a, d) Normalized density of mesoscale organization parameter Ω , and histogram of updraft radius showing mass flux per bin (with a bin size of 100 m) at 1,000 hPa level ((b, e) and 600 hPa level ((c, f) simulated by UNICON and stochastic UNICON during Madden-Julian oscillation phases 4-7 (green) and phases 8-3 (magenta). The mean values of the distributions are denoted at the upper right corner of each plot.

MJO is mainly modulated by the moistening above 850 hPa level. During the active MJO phases, convective updrafts with higher top heights are more frequently generated, consistent with the radar observation of Powell and Houze (2013). Stochastic UNICON produces more frequent shallower convection and stronger mass fluxes in the lower troposphere compared to UNICON (Figures 9b and 9c).

In order to understand the characteristics of cloud population generated by stochastic UNICON, the distributions of mesoscale organization parameter (Ω) and updraft radius (\hat{R}) are drawn (Figure 10). During the active MJO phases, the simulated mesoscale organization parameters are increased by 14% and 7% on average for UNICON and stochastic UNICON, respectively. The increased organization during the active MJO phases is expected to be due to the increased evaporation of convective precipitation during the active MJO phases. Stochastic UNICON simulates generally higher mesoscale organization than UNICON due to the increased downdraft mass flux (Figures 6a and 6d). The (mass-flux weighted) mean updraft radius at 1,000 hPa level is also increased during the active MJO phases since the near-surface updraft radius is an increasing function of the mesoscale organization parameter. Stochastic UNICON shows an updraft radius distribution weighted on small radii which is significantly different from UNICON.

The difference between the updrafts simulated in UNICON and stochastic UNICON is evident in the radius distribution at 600 hPa level (Figures 10c and 10f). UNICON simulates updrafts with larger radii during the active phases, while stochastic UNICON produces similar distributions and mean values of radius between the active and inactive phases. In UNICON, a single bulk plume increases its radius during ascent without being completely detrained, so updrafts with larger radii at the near-surface have larger radii even in upper levels. In contrast, in stochastic UNICON, convective updrafts with small radii are detrained in relatively lower levels, so radius distributions at 600 hPa level become similar. This result reveals the ability of stochastic UNICON to express the coexistence of shallow and deep convection.

Figure 11 shows vertical profiles of tendencies by convection and PBL schemes, all physical processes, and vertical advection during the active and inactive MJO phases. The heating and drying tendencies by convection are greatly enhanced during the active MJO phases. As seen in Figure 6, stochastic UNICON simulates higher heating and drying tendencies by convection compared to UNICON, both during the active and inactive phases. The simulated tendencies by all physical processes are comparable with tendencies from convection and PBL schemes, with the little amount of cooling (up to -2 K day^{-1}) and moistening (up to $0.5 \text{ g kg}^{-1} \text{ day}^{-1}$) being added by stratiform microphysics and radiation schemes. The temperature and specific humidity tendencies by physical processes can be calculated by subtracting advective tendencies from total tendencies and have the

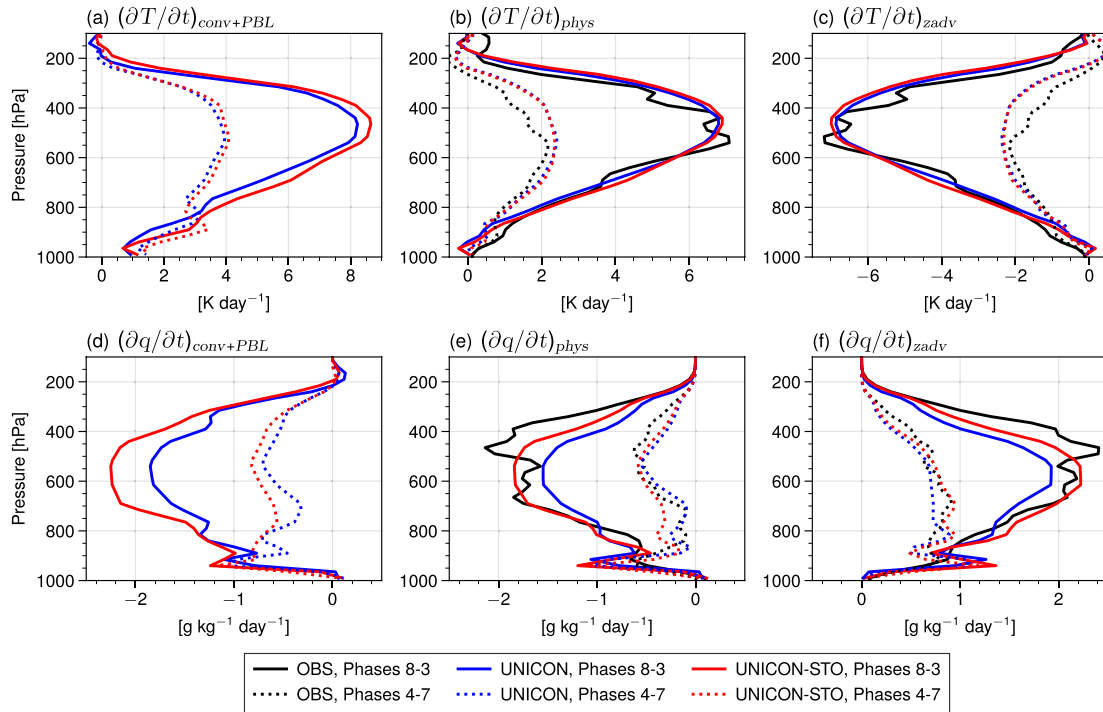


Figure 11. Vertical profiles of time-averaged tendencies of temperature and specific humidity by (a, d) convection and planetary boundary layer schemes, (b, e) all physical processes, and (c, f) vertical advection simulated by UNICON and stochastic UNICON during Madden-Julian oscillation phases 8-3 and phases 4-7 in the DYNAMO-AMIE case. For (b, c, e, f), profiles from observation are also shown.

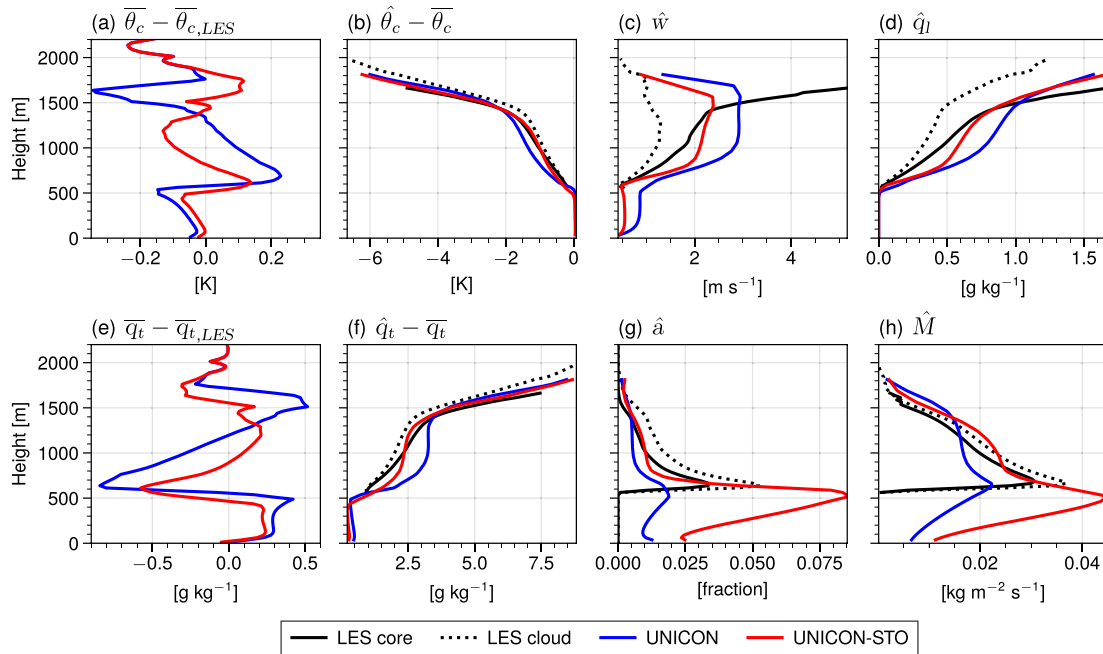


Figure 12. Vertical profiles of (a, e) error of $\bar{\theta}_c$ and \bar{q}_t with respect to large-eddy simulation, (b, f) difference of the moist conserved variables from updrafts with respect to the environmental mean moist conserved variables, (c) updraft vertical velocity, (d) updraft liquid water, (g) updraft fractional area, and (h) updraft fractional mass flux averaged over $t = 4 \sim 6$ hr simulated by UNICON and stochastic UNICON in the BOMEX case.

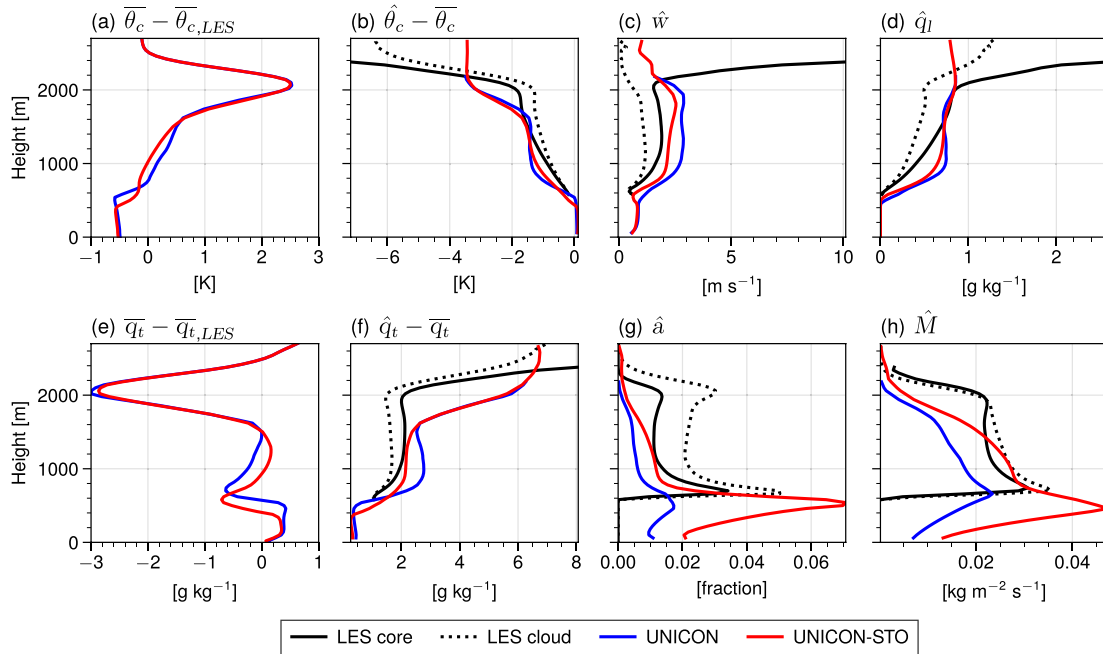


Figure 13. Vertical profiles of (a, e) error of $\bar{\theta}_c$ and \bar{q}_t with respect to large-eddy simulation, (b, f) difference of the moist conserved variables from updrafts with respect to the environmental mean moist conserved variables, (c) updraft vertical velocity, (d) updraft liquid water, (g) updraft fractional area, and (h) updraft fractional mass flux averaged over $t = 20 \sim 24$ hr simulated by UNICON and stochastic UNICON in the RICO case.

same definitions as the apparent heat source (Q_1) and apparent moisture sink (Q_2), respectively. The simulated $(\partial T/\partial t)_{\text{phys}}$ of UNICON and stochastic UNICON closely match with observation during the active phases but are overestimated during the inactive phases. The simulated $(\partial q/\partial t)_{\text{phys}}$ of stochastic UNICON exhibits stronger drying than that of UNICON during the active MJO phases, which is more closely matches with observation. The tendencies by vertical advection are almost inverse of physical tendencies, compensating each other. The increased drying by convection is compensated by the increased moistening by vertical advection in stochastic UNICON, and the net effect of the two is slightly increased moistening, which reduces the dry biases of UNICON.

6.3. Idealized Experiments

In this subsection, results from the idealized SCM experiments are presented and discussed. Figure 12 shows simulated vertical profiles of various updraft properties averaged over $t = 4 \sim 6$ hr in the BOMEX case. UNICON exhibits cold and moist biases in the sub-cloud layer and in the layer 1,300–1,700 m and warm and dry biases in the cloud layer below 1,300 m. Stochastic UNICON reduces these biases, where RMSEs are reduced by 31% and 39% in $\bar{\theta}_c$ and \bar{q}_t profiles, respectively. UNICON shows mass flux with a rapid slope change near the inversion height since the bulk plume in UNICON terminates at a certain height (Figure 12h). Stochastic UNICON simulates a much smoother mass flux profile similar to LES. Stochastic UNICON also simulates $\bar{\theta}_c$ and \bar{q}_t profiles that closely match with the LES cloud and core profiles, while UNICON produces colder and more humid updrafts in the lower cloud layer. UNICON and stochastic UNICON both suffer from rapid increases of \bar{w} and \bar{q}_t in the lower cloud layer, but stochastic UNICON reduces the discrepancy between the profiles from LES and SCM simulations in the cloud layer.

In the RICO case, UNICON displays excessive warm and dry biases near the inversion height of approximately 2,000 m up to >2 K and <-2 g kg⁻¹, respectively (Figure 13). Stochastic UNICON slightly reduces the biases in the cloud layer below the inversion, but the biases near the inversion height are not alleviated. The biases indicate that the inversion heights are underestimated in UNICON and stochastic UNICON. The rapid decrease of $\bar{\theta}_c - \bar{\theta}_c$ (rapid increase of $\bar{q}_t - \bar{q}_t$) near the inversion height in UNICON and stochastic UNICON appears at about 400 m lower heights compared to LES, indicating that convective updrafts terminate at lower levels in the SCM simulations. Here again, UNICON and stochastic UNICON exhibit the rapid increases of \bar{w} and \bar{q}_t in the lower

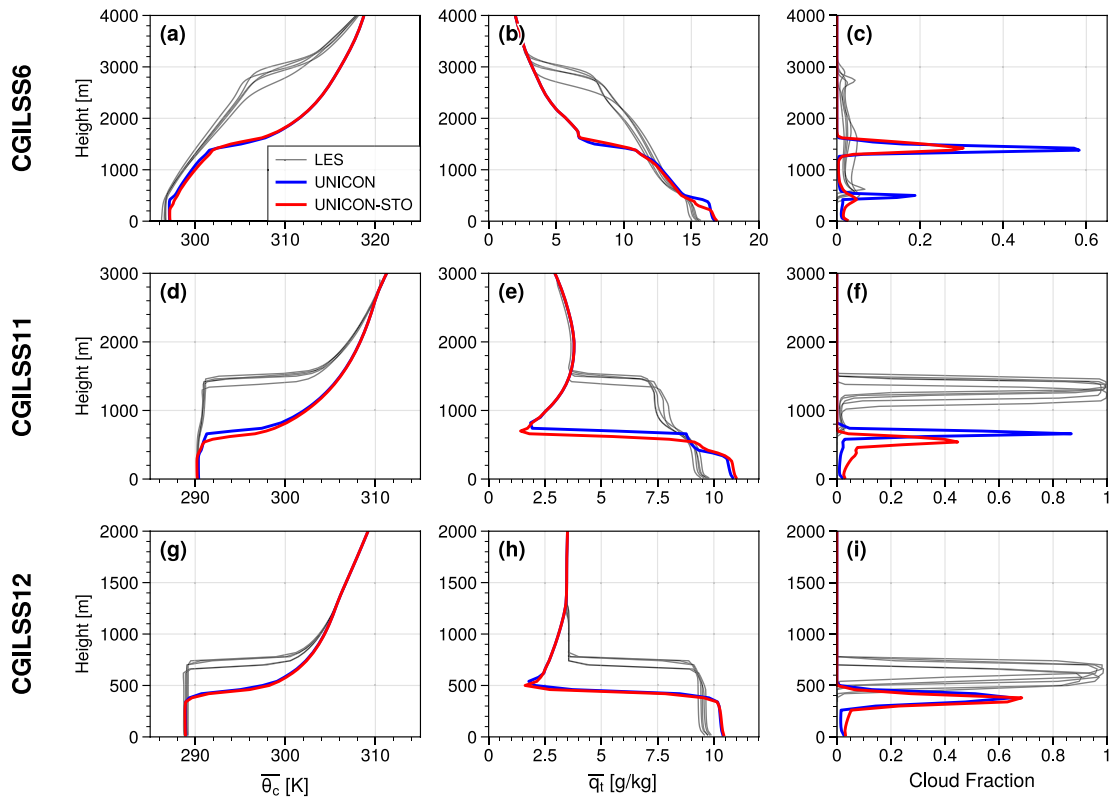


Figure 14. Vertical profiles of (a, d, g) environmental condensate potential temperature, (b, e, h) environmental total water specific humidity, and (c, f, i) cloud fraction averaged over the last day of the simulation period ($t = 216 \sim 240$ hr) simulated by UNICON and stochastic UNICON in the CGILSS6 (first row), CGILSS11 (second row), and CGILSS12 (third row) cases. The profiles of six large-eddy simulation (LES) models from the LES intercomparison study are drawn for reference.

cloud layer. \hat{a} and \hat{M} are underestimated in UNICON, and stochastic UNICON simulates \hat{a} and \hat{M} profiles that better match with LES. However, \hat{a} and \hat{M} are rapidly decreased at lower levels than the LES profiles in both UNICON and stochastic UNICON. As demonstrated by Shin and Baik (2022), the biases presented in the RICO case can be significantly reduced by implementing a stochastic mixing model with a more realistic formula for entrainment and detrainment rates.

Figure 14 shows vertical profiles of environmental moist conserved thermodynamic variables and cloud fraction simulated by UNICON and stochastic UNICON in the CGILSS6, CGILSS11, and CGILSS12 cases. UNICON and stochastic UNICON simulate inversion heights only about half that of LES ensembles and have more humid boundary layers. The PBL scheme of CAM5 (Park & Bretherton, 2009) explicitly includes cloud-top entrainment, but it seems that the cloud-top entrainment is considerably underestimated. Particularly, in the CGILSS6 case, a cumulus cloud layer in the LES models is developed when stratocumulus is formed at the inversion height during days 1–5 and becomes a shallow convection regime (Blossey et al., 2013). In contrast, UNICON and stochastic UNICON failed to develop a cloud layer from decoupled stratocumulus to shallow convection in CGILSS6. Many issues might be associated with simulating realistic feedbacks between radiation, cloud, and boundary-layer turbulence. The intercomparison study of CGILS showed that SCMs have large uncertainties in simulating stratocumulus topped boundary layer (M. Zhang et al., 2013). One possible explanation is that UNICON and stochastic UNICON do not consider downdrafts originated from the inversion. UNICON and stochastic UNICON launch convective updrafts only from the near-surface. However, in the stratocumulus-topped boundary layer, the entrainment of warm and dry tropospheric air, which favors evaporative cooling, contributes to local changes in buoyancy and generates downdrafts at an inversion height. The mass flux of downdrafts is comparable to that of updrafts and has a non-negligible impact on the heat and moisture fluxes within the boundary layer (Davini et al., 2017). The simulated environmental profiles from UNICON and stochastic UNICON are similar in the CGILS cases, while the RMSEs of UNICON are slightly reduced by stochastic UNICON (Table 4). The DYCOMSRF01 case is integrated only for 4 hr, so the environmental thermodynamic profiles simulated

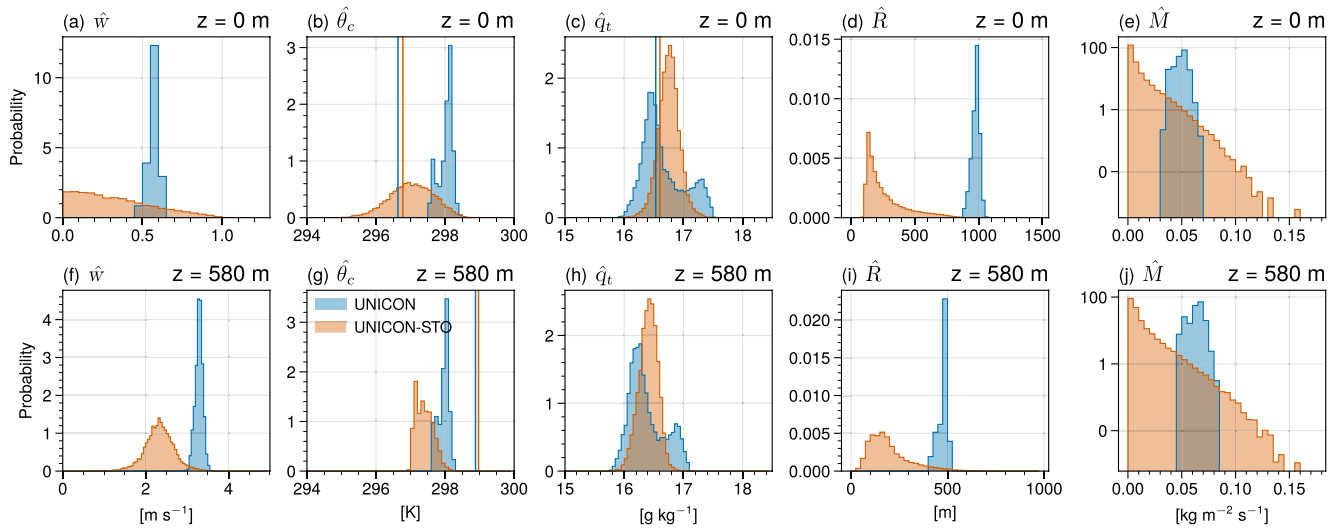


Figure 15. Number probability density function of various updraft properties at the near-surface (first row) and at the cloud-base height of 580 m (second row) simulated by UNICON and stochastic UNICON in the idealized GATE case. The vertical lines in (b, c, and g) denote grid-mean values (θ_c and \bar{q}_t) at each height. Note that the y-axis of (e and j) is in log scale.

from UNICON and stochastic UNICON are almost identical, and not much deviated from the initial profiles (not shown).

6.4. Cloud Variabilities in a Near-Equilibrium Environment

In the time-varying forcing cases, it is difficult to isolate the cloud variabilities that are simulated in stochastic UNICON. In order to get the statistics of cloud variabilities in a near-equilibrium environment of a deep convection regime, an additional SCM simulation of the idealized GATE case is conducted, which uses time-averaged large-scale forcing from the GATEIII observed period. This case is documented in Fu et al. (1995), Khairoutdinov et al. (2009), and Xu et al. (1992). We use the same setting as the time-varying forcing cases for running the case, but the radiation tendency specified in Xu et al. (1992) is used instead of the radiation scheme for this case. In addition, the temperature and moisture profiles are relaxed toward prescribed profiles with a relaxation time scale of $\tau = 6$ hr to avoid drifting of the thermodynamic states. The simulation is run for 90 days, and the statistics of updrafts are collected for the period, excluding the first 10 days.

Figure 15 shows the number PDFs of various updraft properties at the near-surface and the cloud-base height of 580 m. The cloud-base height is defined as the lowest height where the mean updraft liquid water specific humidity (\bar{q}_l) is greater than 0.01 g kg^{-1} . UNICON parameterizes the impact of mesoscale organized flow by adding deterministic perturbation $\Delta\phi_\Omega$ to updraft properties at the near-surface (Equation 2). Therefore, the distributions of \hat{w} and $\hat{\theta}_c$ at the near-surface simulated by UNICON show small variances, with the mean values of approximately 0.5 m s^{-1} and 298 K , respectively (Figures 15a and 15b). The variances are not zero because the cold pool properties simulated by UNICON fluctuate over time and the environment is also not in a perfect equilibrium. The distribution of \hat{q}_t at the near-surface in UNICON shows two peaks and has a relatively large variance because the simulated q_t perturbation by mesoscale organized flow, $\Delta q_{t,\Omega}$, oscillates with two peaks in the UNICON simulation. The oscillation seems to be a numerical issue, but we are unsure about the exact reason. The mean perturbations by mesoscale organized flow simulated by UNICON are $\Delta w_{\Omega} = 0.47 \text{ m s}^{-1}$, $\Delta\theta_{c,\Omega} = 1.34 \text{ K}$, and $\Delta q_{t,\Omega} = -0.057 \text{ g kg}^{-1}$ in the idealized GATE case. The distributions of updraft radius and mass flux at the near-surface also show small variances, with the mean values of $1,000 \text{ m}$ and $0.05 \text{ kg m}^{-2} \text{ s}^{-1}$, respectively.

Compared to UNICON, stochastic UNICON shows larger variances of thermodynamic variables (except \hat{q}_l), updraft radius, and mass flux at the near-surface. This is because stochastic UNICON parameterizes the impact of mesoscale organized flow in a stochastic manner by increasing the variances of the joint PDF of updraft properties. The simulated standard deviations of updraft thermodynamic properties are $\sigma_w^* = 0.47 \text{ m s}^{-1}$, $\sigma_{\theta_c}^* = 0.80 \text{ K}$, and $\sigma_{q_t}^* = 0.19 \text{ g kg}^{-1}$. The distribution of \hat{w} of stochastic UNICON is half Gaussian because the constraint of

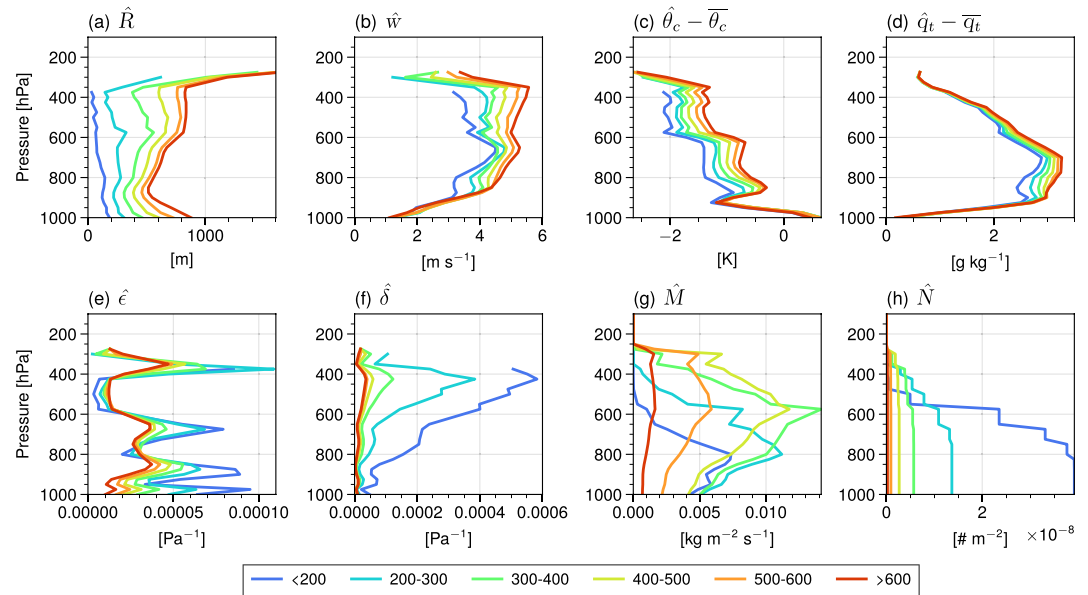


Figure 16. Composite vertical profiles of updraft properties according to the updraft radius at the cloud-base height (shown at the bottom in a unit of meters) obtained from the stochastic UNICON simulation of the idealized GATE case. $\hat{\epsilon}$ and $\hat{\delta}$ are the fractional entrainment and detrainment rates, respectively, and \hat{N} is the number density of updrafts.

$w > 0$ is applied to the multivariate Gaussian. The distributions of $\hat{\theta}_c$ and \hat{q}_t of stochastic UNICON are close to Gaussian. As the updraft radius is parameterized as a power-law distribution with a scale break in stochastic UNICON, the distribution of \hat{R} is weighted on a smaller radius (Figure 15d). Finally, stochastic UNICON reproduces the theoretical exponential distribution of \hat{M} hypothesized by Craig and Cohen (2006). Stochastic UNICON also exhibits larger variabilities of updrafts at the cloud-base height (second row of Figure 15). The shapes of the distributions of \hat{w} and $\hat{\theta}_c$ simulated by stochastic UNICON are deformed at the cloud-base height since the updrafts with relatively smaller \hat{w} and $\hat{\theta}_c$ are detrained in the sub-cloud layer.

The increased variabilities of updrafts in the sub-cloud layer also contribute to increasing variabilities in the cloud layer. Particularly, the updraft radius plays a critical role in generating the cloud layer variabilities. Figure 16 shows composited vertical profiles of updraft properties according to the updraft radius at the cloud-base height, simulated by stochastic UNICON. The wider updrafts tend to have larger \hat{w} , $\hat{\theta}_c$, and \hat{q}_t . The degree of mixing between an updraft and the environment is inversely proportional to the updraft radius in stochastic UNICON. Therefore, the fractional entrainment and detrainment rates are lower for larger updrafts (Figures 16e and 16f). Larger updrafts experience less mixing and have greater buoyancy and vertical velocity. The difference from the shallow convection case is revealed in the relationship between \hat{R} and $\hat{\theta}_c$. In the simulation of the BOMEX case, larger \hat{R} is associated with smaller $\hat{\theta}_c$ due to decreased entrainment (Shin & Park, 2020). However, in the case of deep convection, larger updrafts tend to have larger $\hat{\theta}_c$ since the diabatic heating from the production of precipitation increases in larger updrafts. The updrafts that are small and have low buoyancy have large detrainment rates, so they lose mass flux at lower levels and are consequently detrained at the lower levels (Figures 16g and 16h). The updrafts with radii smaller than 300 m at the cloud-base height can be considered shallow convection, and they have a considerable contribution to total mass flux in the lower troposphere. The improvements in the simulations of the tropical convection cases by stochastic UNICON appear to be related to the representation of shallow convection.

7. Summary and Conclusions

In this study, we extended stochastic UNICON, which was originally formulated for shallow convection, to deep convection by parameterizing the impact of mesoscale organized flow on updraft properties. The extended stochastic UNICON parameterizes thermodynamic properties of updrafts at the near-surface by constructing a joint PDF as multivariate Gaussian distribution. The variances of the joint PDF are the summation of variances

from non-organized turbulence and variances from mesoscale organized flow. The variances of non-organized turbulence are derived from the surface-layer similarity theory, and the variances of mesoscale organized flow are calculated from the UNICON cold pool routine. The distribution of updraft radius is parameterized as a power-law distribution with a scale break, where the scale break radius is parameterized as a linear function of the mesoscale organization parameter. Stochastic UNICON randomly launches multiple convective updrafts from the parameterized distributions at the near-surface to represent different types of convective clouds. The proposed parameterization is validated using a series of LES simulations of radiative-convective equilibrium. The parameterization is able to predict LES-measured standard deviations of convective updrafts for potential temperature and vertical velocity, but not for specific humidity because of the enhancement of water vapor within cold pools. The linear relationship between the mesoscale organization parameter and the scale break radius is also verified using the LES data set.

Four free parameters, c_1 , c_2 , $R_b|_{\Omega=0}$, and $R_b|_{\Omega=1}$, are newly introduced in the formulation of stochastic UNICON. c_1 and c_2 control the variances of thermodynamic properties of updrafts from non-organized turbulence and mesoscale organized flow, respectively, and $R_b|_{\Omega=0}$ and $R_b|_{\Omega=1}$ are scale break radii when the mesoscale organization parameter is 0 and 1, respectively. These four parameters are optimized using SCM simulations of the 10 intensive observation period (IOP) cases over the ocean. A cost function is defined as a weighted sum of RMSEs of moist static energy and surface precipitation rate from the SCM cases simulated by stochastic UNICON, and the cost function is minimized using the Bayesian optimization technique. From the results of the optimization experiment, all four parameters are found to have considerable impacts on the performance of stochastic UNICON. Stochastic UNICON with optimized parameters outperforms original UNICON in most SCM cases, especially for the tropical convection cases. The comparison with the previous versions of stochastic UNICON implies that the performance improvement comes from both stochastic formulations of non-organized turbulence and mesoscale organization. More specifically, parameterizing the stochastic variability of non-organized turbulence improves the simulation of shallow convection and adding the mesoscale organization effect on top of that contributes to improving the simulation of deep convection.

The GATEIII, TOGAII, DYNAMO-AMIE, DYNAMO-North, and DARWIN cases are time-varying forcing experiments that simulate tropical convection, and they are directly compared with IOP observations. In all five cases, stochastic UNICON reduces the negative temperature biases in the upper troposphere and negative moisture biases in the lower troposphere presented in UNICON simulations. The simulations of precipitation rates are also significantly improved by stochastic UNICON, except for the GATEIII case. For the GATEIII, TOGAII, DYNAMO-AMIE, DYNAMO-North, and DARWIN cases, the relative RMSEs (defined as the RMSE of stochastic UNICON divided by the RMSE of UNICON) of moist static energy are 0.780, 0.788, 0.547, 0.588, and 0.759, respectively, and those of precipitation rate are 0.869, 1.003, 0.789, 0.748, and 0.699, respectively. Particularly, during the MJO decaying periods of GATEIII, DYNAMO-AMIE, and DYNAMO-North, the negative temperature biases simulated in UNICON are amplified, and even stochastic UNICON exhibits noticeable negative temperature biases in the upper troposphere. This indicates that anvil clouds and associated stratiform precipitation are not realistically represented in UNICON and stochastic UNICON. The strong negative temperature biases in the upper troposphere during the MJO decaying periods in UNICON produce unrealistically developed convection and overestimate rain peaks during these periods. In the five cases, stochastic UNICON simulates generally increased updraft mass fluxes in the lower troposphere and stronger heating and drying tendencies by convective processes compared to UNICON.

The detailed analysis of simulated MJO in the DYNAMO-AMIE case promotes our understanding of the characteristics of simulated convection. Stochastic UNICON realistically simulates the variations of temperature and moisture anomalies associated with three MJO events during DYNAMO-AMIE, while UNICON fails to reproduce the intensity and timing of the anomalies. During the active MJO phases (8–3 phases), UNICON and stochastic UNICON produce stronger and deeper convection due to higher relative humidity above 850 hPa level compared to the inactive MJO phases (4–7 phases). The simulated mesoscale organization and updraft radius are also greater during the active MJO phases. The difference between UNICON and stochastic UNICON is revealed in the evolution of the updraft population during ascent. In stochastic UNICON, smaller updrafts are detrained at the lower levels due to the spectral representation of convective updrafts. In UNICON, however, a bulk plume increases its size during ascent without complete detrainment. The stronger heating by convection in stochastic UNICON contributes to reducing negative temperature biases in UNICON. The stronger drying tendencies by convection in stochastic UNICON, particularly during the active MJO phases, increase moistening by vertical advection and consequently reduce negative moisture biases in UNICON.

The BOMEX, RICO, CGILSS6, CGILSS11, CGILSS12, and DYCOMSRF01 cases are idealized cases that simulate boundary-layer clouds, and they are compared with LES simulations. The notable improvement by stochastic UNICON is found in the BOMEX case, where stochastic UNICON reduces the RMSE of moist static energy in UNICON by 28% and simulates thermodynamic properties of updrafts more consistent with LES profiles. In the CGILS cases, both UNICON and stochastic UNICON simulate inversion heights only about half of that simulated by LES ensembles, indicating the deficiencies in simulating feedbacks between radiation, clouds, and turbulence for the stratocumulus-topped boundary layer. Finally, the cloud variabilities in the idealized GATE case, which is a near-equilibrium deep convection case, are examined. Stochastic UNICON exhibits enhanced variabilities of thermodynamic variables, radius, and mass flux of updrafts at the near-surface and cloud-base height. The increased variabilities in the sub-cloud layer lead to increased variabilities in the cloud layer, where larger updrafts have higher buoyancy and vertical velocity and experience less detrainment to the environment. The non-negligible contribution of shallow convection is found in the idealized GATE case, suggesting that the improvement in the tropical convection cases by stochastic UNICON is contributed to the representation of the coexistence of shallow and deep convection.

In the near future, we will evaluate the performance of stochastic UNICON in global model simulations. Our study also suggests several important aspects to further improve stochastic UNICON, including a more realistic representation of the life cycle of an MCS and the downdrafts originated from cloud-topped inversion. These issues are also crucial in other convection parameterizations and are subjects that need further study. Finally, although only SCM cases over the ocean were considered in this study, optimization of stochastic UNICON under more general conditions can be expected by adding SCM cases over the continent.

Appendix A: Computation of Mesoscale Perturbations in UNICON

UNICON divides the horizontal grid within the PBL into three regions: cold pools (a_{cp}), uplift region of mesoscale organized flow (a_{Ω}), and the remaining portion where perturbations by mesoscale organized flow are zero ($1 - a_{cp} - a_{\Omega}$). The area-weighted sum of perturbations of a conservative scalar ϕ by mesoscale organized flow of these three regions should be zero:

$$a_{\Omega}\Delta\phi_{\Omega} + a_{cp}\Delta\phi_{cp} = 0, \quad (A1)$$

where $\Delta\phi_{\Omega} = \phi_{\Omega} - \phi_{PBL}$ is the mean perturbation of ϕ in the uplift region of mesoscale organized flow and $\Delta\phi_{cp} = \phi_{cp} - \phi_{PBL}$ is the mean perturbation of ϕ of cold pools (ϕ_{PBL} is the mean ϕ in PBL). a_{Ω} is parameterized as $a_{\Omega} = C_{\Omega}\hat{A}_s$, where $\hat{A}_s = 0.04$ is the net updraft fractional area at the surface and $C_{\Omega} = 5$ is a constant parameter. Therefore, $\Delta\phi_{\Omega}$ is computed as

$$\Delta\phi_{\Omega} = -\frac{a_{cp}\Delta\phi_{cp}}{C_{\Omega}\hat{A}_s}, \quad \phi = \theta_e, q_t, u, v, \xi. \quad (A2)$$

For vertical velocity, it is assumed that a certain fraction of available potential energy in PBL is converted into mesoscale kinetic energy through a convective overturning process. Δw_{Ω} is computed as

$$\Delta w_{\Omega} = a_{cp} \left[\left(\frac{g}{\theta_{v,ref}} \right) \left(\frac{k_* h \theta'_v}{C_{\Omega} \hat{A}_s} \right) \right]^{1/2}, \quad (A3)$$

where $\theta_{v,ref} = 300$ K is the reference virtual potential temperature, $k_* = 0.08$ is the conversion factor of available potential energy, h is the PBL-top height, and θ'_v is the virtual potential temperature difference between cold pools and other area. UNICON assumes that the properties of convective updrafts at the near-surface are modulated by the subgrid mesoscale organized flow. See Section 2d in Park (2014) for detailed derivation.

Appendix B: Temporal Evolutions of Simulated Statistics in the Radiative-Convective Equilibrium Simulations

Figure S2 in Supporting Information S1 shows the time series of the domain-averaged variables simulated in the four radiative-convective equilibrium simulations. As the simulations are initialized from the horizontally averaged profiles of coarser resolution simulations in equilibrium, the convection and mean state of all

simulations rapidly reach equilibrium after about 40 hr without noticeable drifts. The surface air temperature is higher in the order of DEEP4K, DEEP2K, DEEP4K-S, and DEEP2K-S, and the precipitable water is in the same order. To test whether convective self-aggregation occurred in the simulations, we use the interquartile range ($IQR = Q_3 - Q_1$, where Q_1 is the first quartile and Q_3 is the third quartile) of precipitable water to quantify convective self-aggregation, which many studies have used (e.g., Arnold & Randall, 2015; Bretherton et al., 2005; Muller & Held, 2012). IQR of precipitable water is much smaller than the mean precipitable water, indicating that there is no self-aggregation. IQR increases in a 15–100 days time scale when convection aggregates (Wing et al., 2017), but no notable increase is observed in the simulations.

Data Availability Statement

The code of UCLA-LES is open sourced and available at <https://github.com/uclales/uclales>. The single-column model and LES outputs presented in this study are available at <https://doi.org/10.5281/zenodo.7574928>.

Acknowledgments

The authors are grateful to three anonymous reviewers for providing valuable comments on this work. This work was supported by the National Research Foundation of Korea (NRF) under Grant 2021R1A2C1007044 and also supported by the National Supercomputing Center with supercomputing resources including technical support (KSC-2021-CRE-0475).

References

- Arakawa, A., & Schubert, W. (1974). Interaction of a cumulus cloud ensemble with the large-scale environment, Part I. *Journal of the Atmospheric Sciences*, 31(3), 674–701. [https://doi.org/10.1175/1520-0469\(1974\)031<0674:ioacce>2.0.co;2](https://doi.org/10.1175/1520-0469(1974)031<0674:ioacce>2.0.co;2)
- Arnold, N. P., & Randall, D. A. (2015). Global-scale convective aggregation: Implications for the Madden-Julian Oscillation. *Journal of Advances in Modeling Earth Systems*, 7(4), 1499–1518. <https://doi.org/10.1002/2015ms000498>
- Baba, Y. (2019). Spectral cumulus parameterization based on cloud-resolving model. *Climate Dynamics*, 52(1), 309–334. <https://doi.org/10.1007/s00382-018-4137-z>
- Baba, Y. (2021). Improved intraseasonal variability in the initialization of SINTEX-F2 using a spectral cumulus parameterization. *International Journal of Climatology*, 41(15), 6690–6712. <https://doi.org/10.1002/joc.7220>
- Baba, Y., & Giorgetta, M. A. (2020). Tropical variability simulated in ICON-A with a spectral cumulus parameterization. *Journal of Advances in Modeling Earth Systems*, 12(1), e2019MS001732. <https://doi.org/10.1029/2019ms001732>
- Bechtold, P., Köhler, M., Jung, T., Doblas-Reyes, F., Leutbecher, M., Rodwell, M. J., et al. (2008). Advances in simulating atmospheric variability with the ECMWF model: From synoptic to decadal time-scales. *Quarterly Journal of the Royal Meteorological Society*, 134(634), 1337–1351. <https://doi.org/10.1002/qj.289>
- Blossey, P. N., Bretherton, C. S., Zhang, M., Cheng, A., Endo, S., Heus, T., et al. (2013). Marine low cloud sensitivity to an idealized climate change: The CGILS LES intercomparison. *Journal of Advances in Modeling Earth Systems*, 5(2), 234–258. <https://doi.org/10.1002/jame.20025>
- Böing, S. J., Jonker, H. J., Siebesma, A. P., & Grabowski, W. W. (2012). Influence of the subcloud layer on the development of a deep convective ensemble. *Journal of the Atmospheric Sciences*, 69(9), 2682–2698. <https://doi.org/10.1175/jas-d-11-0317.1>
- Bretherton, C. S., Blossey, P. N., & Khairoutdinov, M. (2005). An energy-balance analysis of deep convective self-aggregation above uniform SST. *Journal of the Atmospheric Sciences*, 62(12), 4273–4292. <https://doi.org/10.1175/jas3614.1>
- Cahalan, R. F., & Joseph, J. H. (1989). Fractal statistics of cloud fields. *Monthly Weather Review*, 117(2), 261–272. [https://doi.org/10.1175/1520-0493\(1989\)117<0261:fsocf>2.0.co;2](https://doi.org/10.1175/1520-0493(1989)117<0261:fsocf>2.0.co;2)
- Cai, Q., Zhang, G. J., & Zhou, T. (2013). Impacts of shallow convection on MJO simulation: A moist static energy and moisture budget analysis. *Journal of Climate*, 26(8), 2417–2431. <https://doi.org/10.1175/jcli-d-12-00127.1>
- Cohen, B. G., & Craig, G. C. (2006). Fluctuations in an equilibrium convective ensemble. Part II: Numerical experiments. *Journal of the Atmospheric Sciences*, 63(8), 2005–2015. <https://doi.org/10.1175/jas3710.1>
- Couvreur, F., Hourdin, F., Williamson, D., Roehrig, R., Volodina, V., Villefranche, N., et al. (2021). Process-based climate model development harnessing machine learning: I. A calibration tool for parameterization improvement. *Journal of Advances in Modeling Earth Systems*, 13(3), e2020MS002217. <https://doi.org/10.1029/2020ms002217>
- Craig, G. C., & Cohen, B. G. (2006). Fluctuations in an equilibrium convective ensemble. Part I: Theoretical formulation. *Journal of the Atmospheric Sciences*, 63(8), 1996–2004. <https://doi.org/10.1175/jas3709.1>
- Davini, P., D'Andrea, F., Park, S.-B., & Gentile, P. (2017). Coherent structures in large-eddy simulations of a nonprecipitating stratocumulus-topped boundary layer. *Journal of the Atmospheric Sciences*, 74(12), 4117–4137. <https://doi.org/10.1175/jas-d-17-0050.1>
- Dawe, J. T., & Austin, P. H. (2013). Direct entrainment and detrainment rate distributions of individual shallow cumulus clouds in an LES. *Atmospheric Chemistry and Physics*, 13(2), 5365–5410. <https://doi.org/10.5194/acp-13-7795-2013>
- Deb, K. (2014). Multi-objective optimization. In *Search methodologies* (pp. 403–449). Springer.
- De La Chevrotiere, M., Khouider, B., & Majda, A. J. (2014). Calibration of the stochastic multicloud model using Bayesian inference. *SIAM Journal on Scientific Computing*, 36(3), B538–B560. <https://doi.org/10.1137/13094267x>
- Dunbar, O. R., Garbuno-Inigo, A., Schneider, T., & Stuart, A. M. (2021). Calibration and uncertainty quantification of convective parameters in an idealized GCM. *Journal of Advances in Modeling Earth Systems*, 13(9), e2020MS002454. <https://doi.org/10.1029/2020ms002454>
- Feng, Z., Hagos, S., Rowe, A. K., Burleson, C. D., Martini, M. N., & de Zoeke, S. P. (2015). Mechanisms of convective cloud organization by cold pools over tropical warm ocean during the AMIE/DYNAMO field campaign. *Journal of Advances in Modeling Earth Systems*, 7(2), 357–381. <https://doi.org/10.1002/2014ms000384>
- Fu, Q., Krueger, S. K., & Liou, K. (1995). Interactions of radiation and convection in simulated tropical cloud clusters. *Journal of the Atmospheric Sciences*, 52(9), 1310–1328. [https://doi.org/10.1175/1520-0469\(1995\)052<1310:ioraci>2.0.co;2](https://doi.org/10.1175/1520-0469(1995)052<1310:ioraci>2.0.co;2)
- González, J., Dai, Z., Hennig, P., & Lawrence, N. (2016). Batch Bayesian optimization via local penalization. In *Proceedings of the 19th International Conference on Artificial Intelligence and Statistics* (pp. 648–657). PMLR.
- Gregory, D. (2001). Estimation of entrainment rate in simple models of convective clouds. *Quarterly Journal of the Royal Meteorological Society*, 127(571), 53–72. <https://doi.org/10.1002/qj.49712757104>
- Heus, T., & Seifert, A. (2013). Automated tracking of shallow cumulus clouds in large domain, long duration large eddy simulations. *Geoscientific Model Development*, 6(4), 1261–1273. <https://doi.org/10.5194/gmd-6-1261-2013>

- Hourdin, F., Williamson, D., Rio, C., Couvreux, F., Roechrig, R., Villefranche, N., et al. (2021). Process-based climate model development harnessing machine learning: II. Model calibration from single column to global. *Journal of Advances in Modeling Earth Systems*, 13(6), e2020MS002225. <https://doi.org/10.1029/2020ms002225>
- Houze, R. A., & Betts, A. K. (1981). Convection in GATE. *Reviews of Geophysics*, 19(4), 541–576. <https://doi.org/10.1029/rg019i004p00541>
- Janiga, M. A., & Zhang, C. (2016). MJO moisture budget during DYNAMO in a cloud-resolving model. *Journal of the Atmospheric Sciences*, 73(6), 2257–2278. <https://doi.org/10.1175/jas-d-14-0379.1>
- Johnson, R. H., Ciesielski, P. E., & Rickenbach, T. M. (2016). A further look at Q1 and Q2 from TOGA COARE. *Meteorological Monographs*, 56(1), 1.1–1.12. <https://doi.org/10.1175/amsmonographs-d-15-0002.1>
- Jones, D. R., Schonlau, M., & Welch, W. J. (1998). Efficient global optimization of expensive black-box functions. *Journal of Global Optimization*, 13(4), 455–492. <https://doi.org/10.1023/a:1008306431147>
- Kain, J. S., & Fritsch, J. M. (1990). A one-dimensional entraining/detraining plume model and its application in convective parameterization. *Journal of the Atmospheric Sciences*, 47(23), 2784–2802. [https://doi.org/10.1175/1520-0469\(1990\)047<2784:aodepm>2.0.co;2](https://doi.org/10.1175/1520-0469(1990)047<2784:aodepm>2.0.co;2)
- Khairoutdinov, M. F., Krueger, S. K., Moeng, C.-H., Bogenschutz, P. A., & Randall, D. A. (2009). Large-eddy simulation of maritime deep tropical convection. *Journal of Advances in Modeling Earth Systems*, 1(4), 15. Art. #15. <https://doi.org/10.3894/james.2009.1.15>
- Kuroski, M. J., Suselj, K., & Grabowski, W. W. (2019). Is shallow convection sensitive to environmental heterogeneities? *Geophysical Research Letters*, 46(3), 1785–1793. <https://doi.org/10.1029/2018gl080847>
- Kuroski, M. J., Suselj, K., Grabowski, W. W., & Teixeira, J. (2018). Shallow-to-deep transition of continental moist convection: Cold pools, surface fluxes, and mesoscale organization. *Journal of the Atmospheric Sciences*, 75(12), 4071–4090. <https://doi.org/10.1175/jas-d-18-0031.1>
- Langhans, W., Mueller, J., & Collins, W. D. (2019). Optimization of the eddy-diffusivity/mass-flux shallow cumulus and boundary-layer parameterization using surrogate models. *Journal of Advances in Modeling Earth Systems*, 11(2), 402–416. <https://doi.org/10.1029/2018ms001449>
- Langhans, W., & Romps, D. M. (2015). The origin of water vapor rings in tropical oceanic cold pools. *Geophysical Research Letters*, 42(18), 7825–7834. <https://doi.org/10.1002/2015gl065623>
- Lawrence, M. G., & Rasch, P. J. (2005). Tracer transport in deep convective updrafts: Plume ensemble versus bulk formulations. *Journal of the Atmospheric Sciences*, 62(8), 2880–2894. <https://doi.org/10.1175/jas3505.1>
- Letham, B., Karrer, B., Ottoni, G., & Bakshy, E. (2019). Constrained Bayesian optimization with noisy experiments. *Bayesian Analysis*, 14(2), 495–519. <https://doi.org/10.1214/18-ba1110>
- Lin, X., & Johnson, R. H. (1996). Kinematic and thermodynamic characteristics of the flow over the western Pacific warm pool during TOGA COARE. *Journal of the Atmospheric Sciences*, 53(5), 695–715. [https://doi.org/10.1175/1520-0469\(1996\)053<0695:kacot>2.0.co;2](https://doi.org/10.1175/1520-0469(1996)053<0695:kacot>2.0.co;2)
- Lu, C., Liu, Y., Zhang, G. J., Wu, X., Endo, S., Cao, L., et al. (2016). Improving parameterization of entrainment rate for shallow convection with aircraft measurements and large-eddy simulation. *Journal of the Atmospheric Sciences*, 73(2), 761–773. <https://doi.org/10.1175/jas-d-15-0050.1>
- Mapes, B., & Neale, R. (2011). Parameterizing convective organization to escape the entrainment dilemma. *Journal of Advances in Modeling Earth Systems*, 3(2), M06004. <https://doi.org/10.1029/2011ms000042>
- May, P. T., Mather, J. H., Vaughan, G., Jakob, C., McFarquhar, G. M., Bower, K. N., & Mace, G. G. (2008). The tropical warm pool international cloud experiment. *Bulletin of the American Meteorological Society*, 89(5), 629–646. <https://doi.org/10.1175/bams-89-5-629>
- McKay, M., Beckman, R., & Conover, W. (1979). A comparison of three methods for selecting values of input variables in the analysis of output from a computer code. *Technometrics*, 21(2), 239–245. <https://doi.org/10.1080/00401706.1979.10489755>
- Muller, C. J., & Held, I. M. (2012). Detailed investigation of the self-aggregation of convection in cloud-resolving simulations. *Journal of the Atmospheric Sciences*, 69(8), 2551–2565. <https://doi.org/10.1175/jas-d-11-0257.1>
- Neelin, J. D., Bracco, A., Luo, H., McWilliams, J. C., & Meyerson, J. E. (2010). Considerations for parameter optimization and sensitivity in climate models. *Proceedings of the National Academy of Sciences*, 107(50), 21349–21354. <https://doi.org/10.1073/pnas.1015473107>
- Neggers, R. (2015). Exploring bin-macrophysics models for moist convective transport and clouds. *Journal of Advances in Modeling Earth Systems*, 7(4), 2079–2104. <https://doi.org/10.1002/2015ms000502>
- Neggers, R., Griewank, P., & Heus, T. (2019). Power-law scaling in the internal variability of cumulus cloud size distributions due to subsampling and spatial organization. *Journal of the Atmospheric Sciences*, 76(6), 1489–1503. <https://doi.org/10.1175/jas-d-18-0194.1>
- Neggers, R., Jonker, H., & Siebesma, A. (2003). Size statistics of cumulus cloud populations in large-eddy simulations. *Journal of the Atmospheric Sciences*, 60(8), 1060–1074. [https://doi.org/10.1175/1520-0469\(2003\)60<1060:ssoccp>2.0.co;2](https://doi.org/10.1175/1520-0469(2003)60<1060:ssoccp>2.0.co;2)
- Neggers, R., Siebesma, A., & Jonker, H. (2002). A multiparcel model for shallow cumulus convection. *Journal of the Atmospheric Sciences*, 59(10), 1655–1668. [https://doi.org/10.1175/1520-0469\(2002\)059<1655:ammfsc>2.0.co;2](https://doi.org/10.1175/1520-0469(2002)059<1655:ammfsc>2.0.co;2)
- O'Brien, T. A., Li, F., Collins, W. D., Rauscher, S. A., Ringler, T. D., Taylor, M., et al. (2013). Observed scaling in clouds and precipitation and scale incognizance in regional to global atmospheric models. *Journal of Climate*, 26(23), 9313–9333. <https://doi.org/10.1175/jcli-d-13-00005.1>
- Pan, D.-M., & Randall, D. D. (1998). A cumulus parameterization with a prognostic closure. *Quarterly Journal of the Royal Meteorological Society*, 124(547), 949–981. <https://doi.org/10.1002/qj.49712454714>
- Park, S. (2014). A unified convection scheme (UNICON). Part I: Formulation. *Journal of the Atmospheric Sciences*, 71(11), 3902–3930. <https://doi.org/10.1175/jas-d-13-0233.1>
- Park, S., & Bretherton, C. S. (2009). The University of Washington shallow convection and moist turbulence schemes and their impact on climate simulations with the Community Atmosphere Model. *Journal of Climate*, 22(12), 3449–3469. <https://doi.org/10.1175/2008jcli2557.1>
- Park, S., Shin, J., Kim, S., Oh, E., & Kim, Y. (2019). Global climate simulated by the Seoul National University atmosphere model version 0 with a unified convection scheme (SAM0-UNICON). *Journal of Climate*, 32(10), 2917–2949. <https://doi.org/10.1175/jcli-d-18-0796.1>
- Pathak, R., Dasari, H. P., El Mohtar, S., Subramanian, A. C., Sahany, S., Mishra, S. K., et al. (2021). Uncertainty quantification and Bayesian inference of cloud parameterization in the NCAR single column community atmosphere model (SCAM6). *Frontiers in Climate*, 3, 1–23. <https://doi.org/10.3389/fclim.2021.670740>
- Powell, S. W., & Houze, R. A., Jr. (2013). The cloud population and onset of the Madden-Julian oscillation over the Indian Ocean during DYNAMO-AMIE. *Journal of Geophysical Research: Atmospheres*, 118(21), 11979–11995. <https://doi.org/10.1002/2013jd020421>
- Rasmussen, C. E. (2003). Gaussian processes in machine learning. In *Summer school on machine learning* (pp. 63–71).
- Rauber, R. M., Stevens, B., Ochs, H. T., Knight, C., Albrecht, B. A., Blyth, A. M., et al. (2007). Rain in shallow cumulus over the ocean: The RICO campaign. *Bulletin of the American Meteorological Society*, 88(12), 1912–1928. <https://doi.org/10.1175/bams-88-12-1912>
- Rickenbach, T. M., & Rutledge, S. A. (1998). Convection in TOGA COARE: Horizontal scale, morphology, and rainfall production. *Journal of the Atmospheric Sciences*, 55(17), 2715–2729. [https://doi.org/10.1175/1520-0469\(1998\)055<2715:citchs>2.0.co;2](https://doi.org/10.1175/1520-0469(1998)055<2715:citchs>2.0.co;2)
- Romps, D. M., & Kuang, Z. (2010). Nature versus nurture in shallow convection. *Journal of the Atmospheric Sciences*, 67(5), 1655–1666. <https://doi.org/10.1175/2009jas3307.1>

- Seifert, A., & Beheng, K. D. (2006). A two-moment cloud microphysics parameterization for mixed-phase clouds. Part 1: Model description. *Meteorology and Atmospheric Physics*, 92(1–2), 45–66. <https://doi.org/10.1007/s00703-005-0112-4>
- Seifert, A., & Heus, T. (2013). Large-eddy simulation of organized precipitating trade wind cumulus clouds. *Atmospheric Chemistry and Physics*, 13(11), 5631–5645. <https://doi.org/10.5194/acp-13-5631-2013>
- Shin, J., & Baik, J.-J. (2022). Parameterization of stochastically entraining convection using machine learning technique. *Journal of Advances in Modeling Earth Systems*, 14(5), e2021MS002817. <https://doi.org/10.1029/2021ms002817>
- Shin, J., & Park, S. (2020). A stochastic unified convection scheme (UNICON). Part I: Formulation and single-column simulation for shallow convection. *Journal of the Atmospheric Sciences*, 77(2), 583–610. <https://doi.org/10.1175/jas-d-19-0117.1>
- Siebesma, A. P., Bretherton, C. S., Brown, A., Chlond, A., Cuxart, J., Duynkerke, P. G., et al. (2003). A large eddy simulation intercomparison study of shallow cumulus convection. *Journal of the Atmospheric Sciences*, 60(10), 1201–1219. [https://doi.org/10.1175/1520-0469\(2003\)60<1201:alesis>2.0.co;2](https://doi.org/10.1175/1520-0469(2003)60<1201:alesis>2.0.co;2)
- Stevens, B., Moeng, C.-H., Ackerman, A. S., Bretherton, C. S., Chlond, A., de Roode, S., et al. (2005). Evaluation of large-eddy simulations via observations of nocturnal marine stratocumulus. *Monthly Weather Review*, 133(6), 1443–1462. <https://doi.org/10.1175/mwr2930.1>
- Stevens, B., Moeng, C.-H., & Sullivan, P. P. (1999). Large-eddy simulations of radiatively driven convection: Sensitivities to the representation of small scales. *Journal of the Atmospheric Sciences*, 56(23), 3963–3984. [https://doi.org/10.1175/1520-0469\(1999\)056<3963:lesord>2.0.co;2](https://doi.org/10.1175/1520-0469(1999)056<3963:lesord>2.0.co;2)
- Suselj, K., Kurowski, M. J., & Teixeira, J. (2019). A unified eddy-diffusivity/mass-flux approach for modeling atmospheric convection. *Journal of the Atmospheric Sciences*, 76(8), 2505–2537. <https://doi.org/10.1175/jas-d-18-0239.1>
- Sušelj, K., Teixeira, J., & Chung, D. (2013). A unified model for moist convective boundary layers based on a stochastic eddy-diffusivity/mass-flux parameterization. *Journal of the Atmospheric Sciences*, 70(7), 1929–1953. <https://doi.org/10.1175/jas-d-12-0106.1>
- Tiedtke, M. (1989). A comprehensive mass flux scheme for cumulus parameterization in large-scale models. *Monthly Weather Review*, 117(8), 1779–1800. [https://doi.org/10.1175/1520-0493\(1989\)117<1779:acmfsf>2.0.co;2](https://doi.org/10.1175/1520-0493(1989)117<1779:acmfsf>2.0.co;2)
- Tompkins, A. M. (2000). The impact of dimensionality on long-term cloud-resolving model simulations. *Monthly Weather Review*, 128(5), 1521–1535. [https://doi.org/10.1175/1520-0493\(2000\)128<1521:tiodol>2.0.co;2](https://doi.org/10.1175/1520-0493(2000)128<1521:tiodol>2.0.co;2)
- Tompkins, A. M. (2001). Organization of tropical convection in low vertical wind shears: The role of cold pools. *Journal of the Atmospheric Sciences*, 58(13), 1650–1672. [https://doi.org/10.1175/1520-0469\(2001\)058<1650:ootcil>2.0.co;2](https://doi.org/10.1175/1520-0469(2001)058<1650:ootcil>2.0.co;2)
- Torri, G., Kuang, Z., & Tian, Y. (2015). Mechanisms for convection triggering by cold pools. *Geophysical Research Letters*, 42(6), 1943–1950. <https://doi.org/10.1002/2015gl063227>
- vanZanten, M. C., Stevens, B., Nuijens, L., Siebesma, A. P., Ackerman, A. S., Burnet, F., et al. (2011). Controls on precipitation and cloudiness in simulations of trade-wind cumulus as observed during RICO. *Journal of Advances in Modeling Earth Systems*, 3(2), M06001. <https://doi.org/10.1029/2011MS000056>
- Webster, P. J., & Lukas, R. (1992). TOGA COARE: The coupled ocean–atmosphere response experiment. *Bulletin of the American Meteorological Society*, 73(9), 1377–1416. [https://doi.org/10.1175/1520-0477\(1992\)073<1377:tctcor>2.0.co;2](https://doi.org/10.1175/1520-0477(1992)073<1377:tctcor>2.0.co;2)
- Wheeler, M. C., & Hendon, H. H. (2004). An all-season real-time multivariate MJO index: Development of an index for monitoring and prediction. *Monthly Weather Review*, 132(8), 1917–1932. [https://doi.org/10.1175/1520-0493\(2004\)132<1917:aarmmi>2.0.co;2](https://doi.org/10.1175/1520-0493(2004)132<1917:aarmmi>2.0.co;2)
- Wing, A. A., Emanuel, K., Holloway, C. E., & Muller, C. (2017). Convective self-aggregation in numerical simulations: A review. *Surveys in Geophysics*, 38(6), 1173–1197. <https://doi.org/10.1007/s10712-017-9408-4>
- Wood, R., & Field, P. R. (2011). The distribution of cloud horizontal sizes. *Journal of Climate*, 24(18), 4800–4816. <https://doi.org/10.1175/2011jcli4056.1>
- Xu, K.-M., Arakawa, A., & Krueger, S. K. (1992). The macroscopic behavior of cumulus ensembles simulated by a cumulus ensemble model. *Journal of the Atmospheric Sciences*, 49(24), 2402–2420. [https://doi.org/10.1175/1520-0469\(1992\)049<2402:tmboce>2.0.co;2](https://doi.org/10.1175/1520-0469(1992)049<2402:tmboce>2.0.co;2)
- Yang, B., Wang, M., Zhang, G. J., Guo, Z., Huang, A., Zhang, Y., & Qian, Y. (2021). Linking deep and shallow convective mass fluxes via an assumed entrainment distribution in CAM5-CLUBB: Parameterization and simulated precipitation variability. *Journal of Advances in Modeling Earth Systems*, 13(5), e2020MS002357. <https://doi.org/10.1029/2020ms002357>
- Yano, J.-I., & Plant, R. S. (2020). Why does Arakawa and Schubert's convective quasi-equilibrium closure not work? Mathematical analysis and implications. *Journal of the Atmospheric Sciences*, 77(4), 1371–1385. <https://doi.org/10.1175/jas-d-19-0165.1>
- Yoneyama, K., Zhang, C., & Long, C. N. (2013). Tracking pulses of the Madden–Julian oscillation. *Bulletin of the American Meteorological Society*, 94(12), 1871–1891. <https://doi.org/10.1175/bams-d-12-00157.1>
- Yoshimura, H., Mizuta, R., & Murakami, H. (2015). A spectral cumulus parameterization scheme interpolating between two convective updrafts with semi-Lagrangian calculation of transport by compensatory subsidence. *Monthly Weather Review*, 143(2), 597–621. <https://doi.org/10.1175/mwr-d-14-00068.1>
- Zhang, G., & McFarlane, N. (1995). Sensitivity of climate simulations to the parameterization of cumulus convection in the Canadian climate centre general circulation model. *Atmosphere–Ocean*, 33(3), 407–446. <https://doi.org/10.1080/07055900.1995.9649539>
- Zhang, M., Bretherton, C. S., Blossey, P. N., Austin, P. H., Bacmeister, J. T., Bony, S., et al. (2013). CGILS: Results from the first phase of an international project to understand the physical mechanisms of low cloud feedbacks in single column models. *Journal of Advances in Modeling Earth Systems*, 5(4), 826–842. <https://doi.org/10.1002/2013ms000246>
- Zhang, T., Li, L., Lin, Y., Xue, W., Xie, F., Xu, H., & Huang, X. (2015). An automatic and effective parameter optimization method for model tuning. *Geoscientific Model Development*, 8(11), 3579–3591. <https://doi.org/10.5194/gmd-8-3579-2015>